Periodic homogenization and consistent estimates of transport parameters through sphere and polyhedron packings in the whole porosity range

Claude Boutin, Christian Geindreau

Periodic homogenization and consistent estimates of transport parameters through sphere and polyhedron packings in the whole porosity range

Claude Boutin[1,*] and Christian Geindreau[2]
[1]*Université de Lyon–Ecole Nationale des Travaux Publics de l'Etat–LGM/DGCB, CNRS, 3237 Rue Maurice Audin, 69518 Vaulx-en-Velin, France*
[2]*Laboratoire "Sols, Solides, Structures-Risques" (3S-R), Université de Grenoble, UMR CNRS 5521, BP 53 38041 Grenoble Cedex 9, France*

This paper presents a study of transport parameters (diffusion, dynamic permeability, thermal permeability, trapping constant) of porous media by combining the homogenization of periodic media (HPM) and the self-consistent scheme (SCM) based on a bicomposite spherical pattern. The link between the HPM and SCM approaches is first established by using a systematic argument independent of the problem under consideration. It is shown that the periodicity condition can be replaced by zero flux and energy through the whole surface of the representative elementary volume. Consequently the SCM solution can be considered as a geometrical approximation of the local problem derived through HPM for materials such that the morphology of the period is "close" to the SCM pattern. These results are then applied to derive the estimates of the effective diffusion, the dynamic permeability, the thermal permeability and the trapping constant of porous media. These SCM estimates are compared with numerical HPM results obtained on periodic arrays of spheres and polyhedrons. It is shown that SCM estimates provide good analytical approximations of the effective parameters for periodic packings of spheres at porosities larger than 0.6, while the agreement is excellent for periodic packings of polyhedrons *in the whole range of porosity.*

I. INTRODUCTION

In domains concerned by porous media, such as soils mechanics, petroleum engineering, geophysics, acoustics of noise absorbing materials, the prediction of the physical parameters from the basic morphological information of the medium is of interest for both scientific and industrial fields. Among the usual effective coefficients of importance for transport process, this paper focus on the effective Fickean diffusion, the dynamic permeability driving the fluid mass transport in harmonic regime, the thermal permeability driving the inner heat transport in harmonic regime (thus the effective dynamic compressibility of gases in porous media) and the trapping constant.

The physical origin of the effective coefficients has been established, both by phenomenological or thermodynamic approaches [1–4], and also by micro-macro-approaches using homogenization of periodic media (HPM) as developed by [5–7]. This latter method provides a rigorous way to determine these coefficients numerically on chosen representative elementary volume (REV)'s morphology. For instance, exact analytical expressions are available for thin slits or circular cylinders, parametric studies on periodic lattices of spheres have been done by Sangani and Acrivos [8] and Chapman and Higdon [9] respectively for static and harmonic permeability, while Auriault *et al.*[10] treated the case of high-tortuosity two-dimensional (2D) channels.

In realistic media, the morphology is not precisely known and may be far from idealistic geometry. Further, in practice the estimates given by dimensional analysis are (very) poor. For instance, stating that the permeability is of the order of ϕl^2, requires a quantification of a characteristic size of the pores l which accounts for their geometric complexity. Also, in dynamics, although the viscous (or thermal) boundary layer provides a characteristic length, the effects of the morphology remain essential, as shown by Zhou and Sheng [11]. To overcome this difficulty, the procedure of estimating the properties from reconstructed materials or real porous media has been developed [12].

In between these two extremes (very idealistic or realistic morphology), an alternative is given by the self-consistent method (SCM) that reduces the REV morphology of a porous media to the most basic geometrical information, i.e., the porosity ϕ and the pores size. In this paper, we only consider the self-consistent scheme appropriate for transport properties, which is based on bicomposite spherical pattern made of an internal spherical grain and an external fluid shell that ensures the fluid connectivity. Self-consistent models provide analytical expressions which encapsulate the essential parts of the physics and which are easily parameterizable. For a long time, such modeling has been used for homogenization problems where the local conservation equation takes the symbolic form,

$$\nabla_y \cdot \{A(y)[\nabla_y(\text{variable}) + \nabla_x(\text{variable})]\} = 0, \qquad (1)$$

where ∇, $\nabla\cdot$, and Δ stand for the gradient, the divergence and the Laplacian operators respectively, and as usual notation y and x stands for the microscopic and macroscopic space variables, respectively. This type of problem is encountered in the context of diffusion or elasticity. In those cases the microscopic and macroscopic descriptions have the same form, and the effective parameters are independent of

*Corresponding author; claude.boutin@entpe.fr

any local length scale. In contrast, this approach has been applied more recently to static and dynamic permeability (see Berdichevsky and Cai [13], Thiery and Boutin [14] for fibrous media, Boutin [15], Boutin and Geindreau [16] for granular media). The reason lies in the fact that the problems belong to another class characterized by a local conservation equation of the form,

$$\Delta_y(\text{variable}) + \text{Forcing term} = \text{Inertial term}. \qquad (2)$$

Hence macroscopic description is of a different nature than the local description, and implies parameters intrinsically linked to a local length scale. Note that the trapping constant problem also belongs to this category. In the same spirit, the "cell models" has been used for assessing the permeability and the *thermal* permeability by Tarnow [17] for fibrous media and by Umnova *et al.* [18] for assemblies of spheres.

These elements underline the complementarity of the homogenization of periodic media and the self-consistent approach. Further, it has been shown [16] that both leads to very close results for dilute array of spheres. In this context, the aim of this paper is twofold:

(i) First, to justify the link between the SCM and HPM approaches. This is obtained by the following systematic argument independent of the problem in consideration: the periodicity induces conditions of zero flux and energy through the whole surface of the REV that ensure the energy consistency of the HPM approach. As these latter conditions apply to nonperiodic fields, they can be used in the SCM approach, and, in turn, the consistency requirement is necessarily satisfied. Inversely, this observation leads to infer that the SCM solution may provide an approximation of the local HPM problem, for specific periodic materials such that the microstructure is "close" (in a sense defined hereafter) to the SCM pattern.

(ii) Second, to identify classes of periodic materials for which the SCM estimates are relevant. Two types of periodic microstructure "close" to the SCM pattern are investigated. The classical scheme consists in periodizing the bicomposite pattern. This leads to periodic packings of spheres that overlap at low porosities. The original scheme proposed here, is based on the idea that the SCM solution obtained for a spherical bicomposite pattern should be a good geometrical approximation for fields in a polyhedron bicomposite pattern. This leads to consider periodic packings of polyhedrons that never overlap whatever the porosity is (see Sec. II D). Numerical HPM results compared to analytical SCM expressions demonstrate the excellent agreement for polyhedrons packings on the *whole range of porosity*, while the agreement for the classical spheres packings is limited to the dilute range (say porosity larger than 0.6, i.e., nonoverlapping spheres). Finally, the comparisons between spheres and polyhedrons periodic packings enable to identify the parameters most and less sensitive to the media morphology.

The paper is organized as follows. In Sec. II, periodic and self-consistent methods are briefly recalled, the manner to combine them is exposed and the morphology of the studied media is presented. Sections III–V are, respectively, devoted to diffusion, harmonic flow permeability and harmonic thermal permeability. In these three cases the theoretical results

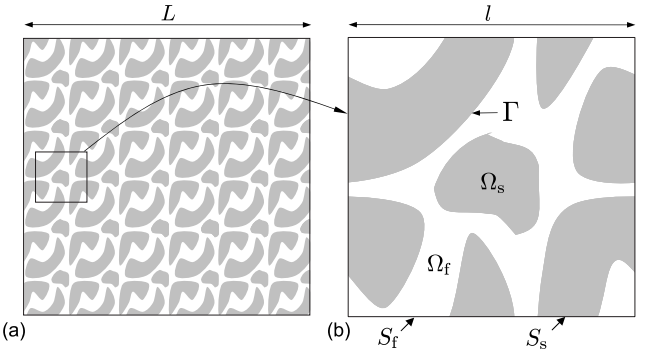

FIG. 1. (a) Macroscopic porous medium, (b) Periodic cell Ω of porous media. Ω_f and Ω_s are respectively the volume of fluid and solid. Γ is the fluid-solid interface inside Ω. S_f and S_s are the fluid and the solid boundaries on $\partial\Omega$.

of homogenization and the self-consistent estimates are first recalled. Then calculations performed on regular assemblies of spheres and of polyhedrons, are presented, discussed, and compared to SCM analytical estimates.

II. HOMOGENIZATION METHODS AND STUDIED POROUS MEDIA

The macroscopic representation of heterogeneous media makes sense only if there is a scale separation. This implies that [19], (i) the material is regular enough to be described by a representative elementary volume (REV) of characteristic size l, and (ii) the physical variables driving the phenomenon varies according to a size L much larger than l.

A. Asymptotic two-scale homogenization

In the asymptotic two-scale homogenization method the above requirements are mathematically introduced. First, the existence of a representative elementary volume is expressed by assuming a periodic material made of identical cells Ω of characteristic size l (Fig. 1). Second, to describe the variations at the well distinct lengths L and l, two spatial variables are introduced, $\mathbf{x}$ for the macroscopic variations, $\mathbf{y}$ for the microscopic variations, $\mathbf{x}$ and $\mathbf{y}$ being related by the scale ratio:

$$\varepsilon = l/L \ll 1, \quad \mathbf{y} = \varepsilon^{-1}\mathbf{x}.$$

The small parameter ε suggests to look for physical unknowns q in the form of asymptotic expansions in powers of ε. As the material periodicity and the scale separation induce the same periodicity for the physical quantities, all the terms are Ω-periodic according to the variable $\mathbf{y}$,

$$q(\mathbf{x},\mathbf{y}) = \sum_0^\infty \varepsilon^i q^i(\mathbf{x},\mathbf{y}) \quad \text{with} \quad q^i(\mathbf{x},\mathbf{y})\Omega - \text{periodic in } \mathbf{y}. \qquad (3)$$

The method consists in introducing the expansions in the two-variable rescaled equations which govern the physics at the local scale (i.e., equations where the dimensionless numbers are quantified in powers of ε, and where the common

spatial derivative is transformed into $\varepsilon^{-1}\partial_y+\partial_x$), then identifying the terms of the same power in ε, and finally solving the boundary value problems obtained in series. The leading order behavior and effective coefficients are derived from the first nontrivial balance equation. The energy consistency between micro and macro descriptions is established through the method.

B. Self-consistent approach

The self-consistent approach enables to conjecture the effective coefficients of heterogeneous media [20]. The method consists in assuming the nature of the macroscopic behavior, then considering a generic pattern representative of the morphology undergoing the local physics of the phenomenon, and finally solving the problem in the pattern submitted to homogeneous macroscopic forcing term. By expressing the energy equivalence between the generic pattern and the equivalent medium, one deduces the macroscopic coefficients.

C. Combining periodic and self-consistent approach

The HPM enables, (i) to derive rigorously the macroscopic behavior from the equations at the pore scale and (ii) to give the theoretical expression of the macroscopic coefficients whatever the periodic microstructure is. However the quantification of these coefficients needs numerical computations. Thus identifying relationships between coefficients and microstructure requires numerous simulations. Complementary to HPM, the interest of SCM is to propose plausible values. They are based on analytical solutions in simplified configurations assumed to capture the salient morphologic features of the REV. If the basic analytical solution is exact, the application of the result to real media is generally conjectured [21], since, conversely to HPM, only a generic pattern and not the actual microstructure is treated.

Nevertheless it is possible to exploit the principles identified by HPM in the framework of the SCM. The HPM shows that the effective parameters result form the *mean* of local fields (or flux) driven from the physics and REV geometry. Since the averaging acts as a numerical filter, the effective parameter contains less information than the local field. This leads to infer that fields, solution of a local "ersatz" problem defined on generic patterns conform to the basic morphological information (proportions, connexity, size), respecting the same physics and close boundary conditions (in the sense detailed below), would give an approximation of exact field and, after averaging, an acceptable estimates of the effective parameter.

The main difficulty in defining an appropriate local problem, "ersatz" of the rigorous problem derived by the HPM, lies in the formulation of "close" boundary conditions. In other words, the periodicity conditions have to be substituted by other conditions which respect the upscaling principles identified by the HPM. To answer this question, recall that the periodicity assumption is the simplest mathematical way to traduce the physical notion of REV. Recall also that, because of the necessary scale separation, the periodicity of the geometry is reported to the physical variables. As a consequence, the whole flux of variables and energy through the boundary of the period are null. This plays an essential role in the HPM up-scaling, permitting to establish the macrodescription (from compatibility equations) and the energy consistency. These arguments give rise to the idea that, to transpose the essential consequence of the periodicity into the local "ersatz" problem, it is sufficient to state that the whole flux of variables and energy through boundary vanish. This approach is interesting when the "ersatz" problem can be solved analytically which induce to consider bicomposite spherical pattern.

The precise developments of this procedure relating HPM and SCM, are detailed in the next sections for the different transport parameters (assuming in addition the macroscopic isotropy). It enables to recover the self-consistent estimates as established by Hashin [20] for the diffusion, by Berdichevsky and Cai [13] and Boutin and Geindreau [16] for the permeability.

D. Studied families of porous media

In the following, the periodic homogenization is applied to porous media made of simple cubic, body-centered cubic, and faced-centered cubic periodic arrays of solid inclusions. According to the nature of inclusions two families of media are considered (Fig. 2).

The first family consists in arrays of nonoverlapping and overlapping solid spheres of the same radius R_i (Fig. 2). These periodic lattices of spheres, labeled (SC), (BCC), and (FCC), are ranging from dilute systems with isolated spheres to highly concentrated consolidated media. The transition between nonoverlapping and overlapping spheres occurs at porosity of 0.47, 0.32, and 0.26 for the (SC), (BCC), and (FCC) microstructure, respectively.

The second family consists in periodic arrays of solid polyhedrons. These arrays, labeled (CC), (TO), and (RD), are built observing that each kind of packing determine a specific polyhedral volume whose periodic reproduction according to the corresponding type of array realize a full paving of the space. Precisely, the three arrays, (CC), (TO), and (RD), based on a cubic volume a^3, are, respectively, associated to a cube (six identical square faces, volume a^3), a truncated octahedron (six square faces and eight hexagonal faces, volume $a^3/2$) and a rhombic dodecahedron (12 identical diamond square faces, volume $a^3/4$) (Fig. 2). Hence, the solid polyhedral inclusions are homothetic to the polyhedral volume associated to the array. These lattices of polyhedrons range from dilute systems to highly concentrated media, but, conversely to spheres packing, the inclusions are isolated in the fluid phase whatever the solid concentration is. Solving boundary value problems arising from the homogenization process provide the effective parameters of such microstructures.

As for the SCM estimates, the self-consistent scheme based on a bicomposite spherical pattern is considered (Fig. 3). The composite sphere Ω of radius R, is constituted by an inner solid sphere Ω_s of radius $R_s=\beta R$ surrounded by a spherical shell Ω_f ($R_s<r<R$) filled by the fluid. The porosity is $\phi=\Omega_f/\Omega=1-\beta^3$. Analytical results will be compared

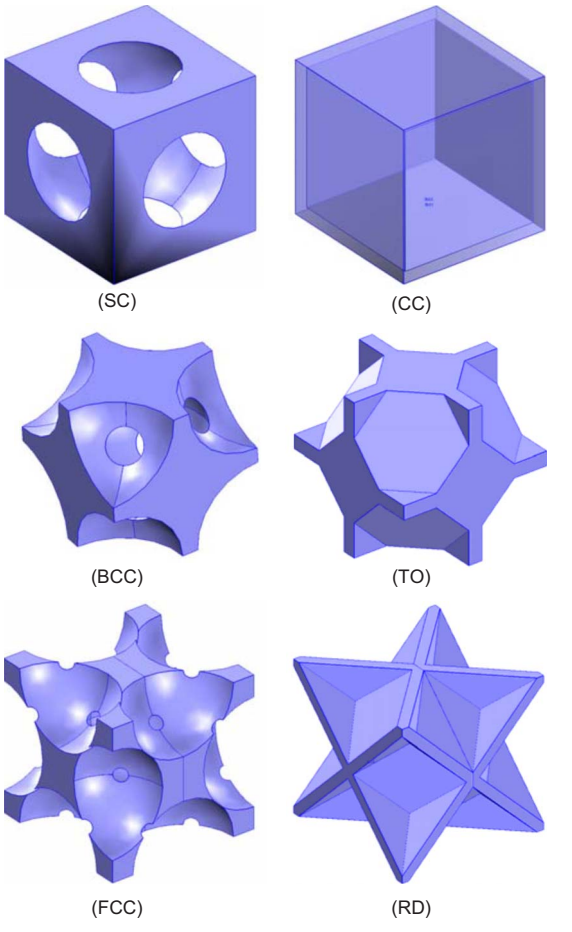

FIG. 2. (Color online) Periodic lattices of spheres: (SC) simple cubic, (BCC) body-centered cubic, (FCC) face centered cubic, and periodic lattices of polyhedrons: (CC) cubic-cubic, (TO) truncated octahedron, (RD) rhombic dodecahedron. The porosity is 0.25.

to the with finite element numerical results obtained on spheres and polyhedrons packings presenting the same porosity and volume of inclusion as the bicomposite spherical pattern.

The three planar symmetry of the arrays and of the spherical pattern imposes the isotropy of the second rank tensors of diffusion or permeability. Therefore, the comparison of the results simply concerns scalar effective coefficients.

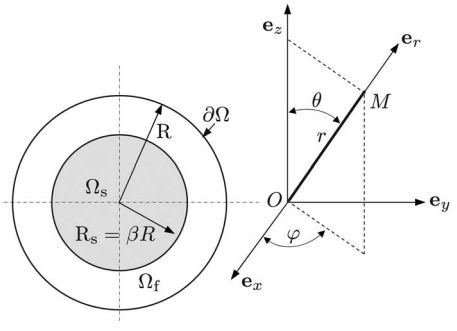

FIG. 3. Bicomposite sphere Ω of radius R constituted by an inner sphere Ω_s surrounded by a spherical shell Ω_f filled of fluid.

III. EFFECTIVE DIFFUSION

A. Homogenization of diffusion in porous media

The Fickean diffusion of a solute at concentration c in a saturated porous media as described in Fig. 1, is governed by the flux balance in the pores Ω_f and the zero flux at the fluid-solid interface Γ,

$$\nabla \cdot [D \nabla c] = 0 \quad \text{in } \Omega_f, \tag{4a}$$

$$D \nabla c \cdot \mathbf{n} = 0 \quad \text{on } \Gamma, \tag{4b}$$

where D is the molecular diffusion coefficient and $\mathbf{n}$ is the outward normal to Γ. The homogenization of diffusion in porous media has been already treated in the past [7]. Here, we only recall the main results necessary for the sequel. The first problem ($4a-\varepsilon^{-2}$, $4b-\varepsilon^{-1}$) associated to the periodicity condition yields to a constant concentration in the pores,

$$c^0(\mathbf{x},\mathbf{y}) = c^0(\mathbf{x}).$$

At the next order, the Ω-periodic concentration c^1 is derived from equations ($4a-\varepsilon^{-1}$, $4b-\varepsilon^{0}$),

$$\nabla_y \cdot [D(\nabla_y c^1 + \nabla_x c^0)] = 0 \quad \text{in } \Omega_f, \tag{5a}$$

$$D(\nabla_y c^1 + \nabla_x c^0) \cdot \mathbf{n} = 0 \quad \text{on } \Gamma. \tag{5b}$$

This set defines the local problem of the form of Eq. (1) where $\nabla_x c^0$ acts as a forcing term. The solution reads [7]

$$c^1(\mathbf{x},\mathbf{y}) = \boldsymbol{\xi}(\mathbf{y}) \cdot \nabla_x c^0 + \bar{c}^1(\mathbf{x}); \quad \boldsymbol{\xi} = \xi^i \mathbf{e}_i, \tag{6}$$

where ξ^i are the three concentrations distributions of zero mean value corresponding to unit concentration gradient in the three directions, $\nabla_x c^0 = \mathbf{e}_i$.

Macroscopic description. The macroscopic description arises from the compatibility of the balance equation at the next order: integrating ($4a-\varepsilon^0$) over Ω_f, then using the zero flux condition on Γ ($4b-\varepsilon$) and the Ω-periodicity, yields:

$$\nabla_x \cdot [\langle D(\nabla_y c^1 + \nabla_x c^0)\rangle] = 0 \quad \text{or} \quad \nabla_x \cdot [\mathbf{D}^{\text{eff}} \cdot \nabla_x c^0] = 0,$$

where here and in the following: $\langle - \rangle$ denotes the average over the representative volume $|\Omega|^{-1}\int_{\Omega_f} - dv$. The effective diffusion tensor is given by

$$\mathbf{D}^{\text{eff}} \cdot \nabla_x c^0 = \langle D(\nabla_y \xi \cdot \nabla_x c^0 + \nabla_x c^0)\rangle, \tag{7}$$

thus

$$\mathbf{D}^{\text{eff}} = \langle D(\nabla_y \xi + \mathbf{I})\rangle, \tag{8}$$

where $\mathbf{I}$ is the unit tensor.

Energy consistency. The consistency between the microscopic and macroscopic descriptions is derived [7] by taking the product of the flux balance ($4a-\varepsilon^{-1}$) by the field c^1. After integrating over the fluid domain Ω_f, then, using the divergence theorem, one obtains

$$\langle \nabla_y \cdot [D(\nabla_y c^1 + \nabla_x c^0)] c^1 \rangle = -\langle D(\nabla_y c^1 + \nabla_x c^0) \cdot \nabla_y c^1 \rangle + \int_{\partial\Omega_f} D(\nabla_y c^1 + \nabla_x c^0) \cdot \mathbf{n} c^1 ds = 0.$$

The boundary $\partial\Omega_f$ of the pores consists into the fluid-solid interface Γ and the fluid boundary $S_f=\partial\Omega_f-\Gamma$ of $\partial\Omega$ (Fig. 1). Thus, the surface integral vanishes because of the zero flux condition on Γ and the periodicity on S_f. Consequently, we get

$$\langle D(\nabla_y c^1+\nabla_x c^0)\cdot(\nabla_y c^1+\nabla_x c^0)\rangle = \langle D(\nabla_y c^1+\nabla_x c^0)\rangle\cdot\nabla_x c^0=\nabla_x c^0\cdot\mathbf{D}^{\text{eff}}\cdot\nabla_x c^0. \quad (9)$$

This establishes the energy consistency between the microscopic and macroscopic descriptions: the energy in the periodic cell is identical to the energy in the same volume of the macroscopic model. Note that this result requires the periodicity to enforce that

$$\int_{\partial\Omega_f-\Gamma} D(\nabla_y c^1+\nabla_x c^0)\cdot\mathbf{n}c^1 ds=0. \quad (10)$$

Equation (10) insures that the energy consistency is satisfied and will be used hereafter in the self-consistent approach.

B. Consistent estimate of effective diffusion

1. Setting of the local diffusion problem

The bicomposite sphere Ω (Fig. 3) is submitted to an imposed macroscopic gradient of concentration $\mathbf{G}=G\mathbf{e}_z$. We use spherical coordinates $(r,\ \theta,\ \varphi)$, with the origin at the center of the spheres and the $\theta=0$ axis given by $\mathbf{e}_z$. The actual concentration in Ω_f is decomposed into the concentration related to the macroscopic gradient, i.e., $\mathbf{r}\cdot\mathbf{G}$ and a local concentration denoted $\tilde{c}$. The balance equation and the inner boundary condition over Γ are those derived by homogenization. The missed condition of periodicity is replaced by the energy consistency condition (10),

$$\nabla\cdot[D(\nabla\tilde{c}+\mathbf{G})]=D\triangle\tilde{c}=0 \quad \text{in } \Omega_f(R_s\le r\le R), \quad (11a)$$

$$D(\nabla\tilde{c}+\mathbf{G})\cdot\mathbf{n}=0 \quad \text{on } \Gamma(r=R_s), \quad (11b)$$

$$\int_{\partial\Omega_f-\Gamma}[D(\nabla\tilde{c}+\mathbf{G})\cdot\mathbf{n}]\tilde{c}ds=0 \quad \text{on } \partial\Omega(r=R). \quad (11c)$$

The consistent estimate of the isotropic effective diffusion denoted $\mathbf{D}^{\text{eff}}=\tilde{D}\mathbf{I}$ is deduced from the mean flux accordingly to Eq. (7),

$$\tilde{D}\mathbf{G}=\frac{1}{\Omega}\int_{\Omega_f} D(\nabla\tilde{c}+\mathbf{G})dv.$$

2. Estimate of the effective diffusion

The resolution of the set Eqs. (11a)–(11c) begin by determining the form of the local field of concentration. To account for isotropy of the space and considering the spherical symmetry of the system, $\tilde{c}$ must be an isotropic function of *both* the forcing gradient $\mathbf{G}$ and the position vector $\mathbf{r}$. Hence, using the tensor theory [22], $\tilde{c}$ necessarily takes the form,

$$\tilde{c}=\mathcal{F}(\mathbf{r}\cdot\mathbf{r},\mathbf{G}\cdot\mathbf{G},\mathbf{r}\cdot\mathbf{G}).$$

Taking into account of the linear dependence on $G=|\mathbf{G}|$, $\tilde{c}$ becomes

$$\tilde{c}=\mathbf{r}\cdot\mathbf{G}f(r)=G\cos(\theta)f(r),$$

whence

$$\nabla\tilde{c}=G\left[f'\cos(\theta)\mathbf{e}_r-\frac{f}{r}\sin(\theta)\mathbf{e}_\theta\right].$$

This result reported in Eq. (11a) provides the differential equation $\Delta[f(r)]=0$, so that $f(r)=a\frac{r}{R}+b\frac{R^2}{r^2}$ where a and b are two constants obtained by expressing the zero flux on Γ Eq. (11b) and the consistency condition (11c),

$$-[f'(\beta R)+1]\cos(\theta)=0, \quad (12a)$$

$$(4\pi/3)[f'(R)+1]f(R)=0. \quad (12b)$$

The consistency condition imposes that $f(R)[f'(R)+1]=0$. The solution $f'(R)+1=0$ means that $\nabla\tilde{c}+G\mathbf{e}_z=0$ in Ω_f, i.e., a zero total flux, hence a zero effective diffusion which is not physically acceptable. Thus, the consistency condition is reduced to $f(R)=0$, i.e., $\tilde{c}(R)=0$, and the set Eqs. (12a) and (12b) is written: $a-2b\beta^{-3}=-R$ and $a+b=0$. Finally, we get

$$f(r)=a\left(\frac{r}{R}-\frac{R^2}{r^2}\right) \quad \text{with} \quad a=-\frac{R}{1+2\beta^{-3}}.$$

Consequently,

$$\frac{1}{\Omega}\int_{\Omega_f}\nabla\tilde{c}dv=\frac{1}{\Omega}\int_{\partial\Omega_f}\tilde{c}\mathbf{n}ds = -\frac{2\pi(\beta R)^2}{\Omega}Gf(\beta R)\int_0^\pi\cos(\theta)\sin(\theta)d\theta\mathbf{e}_r = \frac{\beta^3-1}{1+2\beta^{-3}}G\mathbf{e}_r,$$

therefore

$$\tilde{D}=\frac{1}{\Omega}\int_{\Omega_f}D\left(\frac{1}{G}\nabla\tilde{c}+1\right)dv=D(\beta^3-1)\left(\frac{1}{1+2\beta^{-3}}-1\right).$$

Thus we are left with the self-consistent estimate of the effective diffusion established by Hashin [20] following a slightly different procedure:

$$\tilde{D}=D\frac{2\phi}{3-\phi}. \quad (13)$$

Note that since $\tilde{c}(R)=0$, the actual concentration on the external boundary $\partial\Omega$ is exactly the one given by the forcing gradient $\mathbf{G}$. Further, the total flux on $\partial\Omega$ is given by

$$D[\nabla\tilde{c}+G\mathbf{e}_z]\cdot\mathbf{e}_r=DG\left(\frac{3a}{R}+1\right)\cos(\theta)=\tilde{D}\mathbf{G}\cdot\mathbf{e}_r.$$

Thus, the actual flux on the external boundary $\partial\Omega$ is exactly the flux due to the forcing gradient $\mathbf{G}$ in the homogeneous equivalent media of diffusion coefficient $\tilde{D}$. Consequently, the composite sphere is submitted to the homogeneous conditions in concentration gradient and flux that would exist in the equivalent media. We recover here the usual self-consistent approach were these conditions of continuity be-

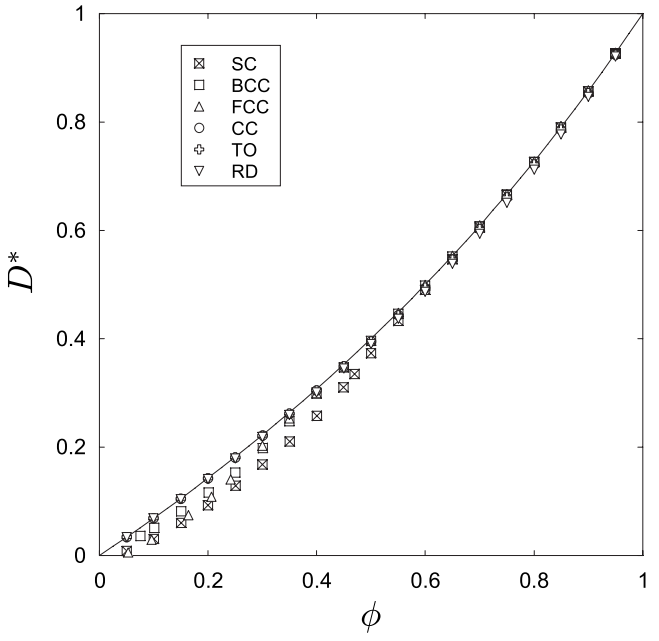

FIG. 4. Dimensionless effective diffusion coefficient $D^*=\widetilde{D}/D$ versus porosity ϕ. Comparison between self-consistent estimate [Eq. (13)] (continuous line) and numerical results for the different packings of spheres and polyhedrons (marks).

tween the bicomposite sphere and equivalent media are supposed at first [20]. These homogeneous conditions at the border of the bicomposite pattern imply that the consistent estimate is an *exact* value for ordered or disordered media made of a packing of homothetic bicomposite spheres filling all the space.

C. Estimates versus numerical values on spheres and polyhedrons packings

The effective diffusion $\widetilde{D}$ of the different arrays of spheres and polyhedrons (Fig. 2) have been computed by solving over a period the boundary value problem (5a–5b) arising from the homogenization process using a finite element code (ComsolMultiphysics). Due to the symmetry of both families of microstructures, numerical simulations have been perform on 1/16 of the total REV. The obtained results and the consistent estimate Eq. (13) are presented on the Fig. 4.

It is worth to notice the excellent agreement between the consistent estimate and numerical values in the *whole range of the porosity* for the polyhedron arrays independently of type of arrangement and thus of the geometry of the inclusion. The agreement is also excellent for dilute arrays of spheres, but discrepancies appear as soon as the spheres overlap. Compared to the consistent estimate, the effective diffusion may significantly be reduced specially at low porosity.

These results are supported by the physical intuition that, on the whole range of porosity, the bicomposite pattern is a better geometrical approximation of periodic polyhedron arrays than of periodic sphere arrays. They also prove that the obstacle made by overlapping areas of spheres sufficiently modifies the flux distribution, which affects the effective diffusion. Besides, the fact that regular packing of identical cubes, truncated octahedrons or rhombic dodecahedrons leads to the same effective parameter than ordered or disordered packing of multidisperse bicomposite spheres of the same porosity illustrates the limited morphological information contained in the effective diffusion coefficient.

IV. DYNAMIC PERMEABILITY

A. Recall of homogenization results for the permeability

The derivation of the dynamic Darcy law from the HPM was established by Levy [23] and Auriault [7], and the sequel recalls the mains results in the case of a rigid porous media saturated by an incompressible fluid. Consider a porous media (Fig. 1) of porosity ϕ, saturated by a fluid of dynamic viscosity μ and density ρ, submitted to small harmonic perturbations of frequency $f=\omega/2\pi$. In harmonic laminar regime, the flow in the pores is described by the incompressibility Eq. (14a), the linearized Navier-Stokes Eq. (14b) and the adherence condition on the fluid—solid interface Γ Eq. (14c),

$$\boldsymbol{\nabla}\cdot\mathbf{v}=0 \quad \text{in } \Omega_f, \tag{14a}$$

$$-\boldsymbol{\nabla}p+\boldsymbol{\nabla}\cdot[2\mu\mathbf{D}(\mathbf{v})]=i\omega\rho\mathbf{v} \quad \text{in } \Omega_f, \tag{14b}$$

$$\mathbf{v}=\mathbf{0} \quad \text{on } \Gamma, \tag{14c}$$

where p, $\mathbf{v}$, and $\mathbf{D}(\mathbf{v})$ stand, respectively, for the pressure, the fluid velocity, and the strain rate tensor, and in which the term $e^{+i\omega t}$ is omitted. The dynamic Darcy regime is reached when the pressure gradient, the viscous forces and the inertial forces are all of the same order of magnitude, i.e.,

$$\mathcal{O}(\boldsymbol{\nabla}p)=\mathcal{O}(\boldsymbol{\nabla}\cdot[2\mu\mathbf{D}(\mathbf{v})])=\mathcal{O}(i\omega\rho\mathbf{v}). \tag{15}$$

The pores' geometry and the adherence condition enforce the velocity to vary at the pore scale. Therefore a macroscopic description requires the pressure to vary at the macro scale. Hence

$$\mathcal{O}(\boldsymbol{\nabla}p)=p/L, \quad \mathcal{O}(\boldsymbol{\nabla}\cdot[2\mu\mathbf{D}(\mathbf{v})])=\mu v/l^2, \quad \mathcal{O}(i\omega\rho\mathbf{v})=\omega\rho v,$$

so that with Eq. (15), the viscous layer and the pore size are of the same order,

$$\delta_v=\sqrt{\mu/(i\rho\omega)}=\mathcal{O}(l).$$

Such a physics of the flow is specified by rescaling Eq. (14b) as follows:

$$-\boldsymbol{\nabla}p+\varepsilon^2\boldsymbol{\nabla}\cdot[2\mu\mathbf{D}(\mathbf{v})]=i\omega\rho\mathbf{v}. \tag{16}$$

The homogenization is applied to Eqs. (14a), (14c), and (16). First, Eq. (16) at the order ε^{-1} reduces to $-\boldsymbol{\nabla}_y p^0=0$ giving a constant pressure in the pores,

$$p^0(\mathbf{x},\mathbf{y})=P(\mathbf{x}).$$

Then, the Ω-periodic velocity $\mathbf{v}^0$ and pressure p^1 are derived from (16$-\varepsilon^0$, 14a$-\varepsilon^{-1}$, 14c$-\varepsilon^0$),

$$-\boldsymbol{\nabla}_y p^1-\boldsymbol{\nabla}_x P+\boldsymbol{\nabla}_y\cdot[2\mu\mathbf{D}_y(\mathbf{v}^0)]=i\omega\rho\mathbf{v}^0 \quad \text{in } \Omega_f, \tag{17a}$$

$$\nabla_y \cdot \mathbf{v}^0 = 0 \quad \text{in } \Omega_f, \tag{17b}$$

$$\mathbf{v}^0 = 0 \quad \text{on } \Gamma. \tag{17c}$$

This set of Eqs. (17), in the form of Eq. (2), defines the linear dynamic permeability problem where $\nabla_x P$ acts as a forcing term. The solution reads [7]

$$\mu \mathbf{v}^0(\mathbf{x},\mathbf{y}) = -\mathbf{k}^i \cdot \nabla_{xi} P, \quad p^1(\mathbf{x},\mathbf{y}) = \zeta^i \cdot \nabla_{xi} P + \widehat{p^1}(\mathbf{x}), \tag{18}$$

where $(-\mathbf{k}^i, \zeta^i)$ are the three complex velocities and pressure distributions corresponding to unit pressure gradient in the three directions, $\nabla_x P = \mathbf{e}_i$.

Macroscopic description. The macroscopic mass balance is derived by integrating $(14a-\varepsilon^0)$ over the pore volume,

$$\int_{\Omega_f} [\nabla_y \cdot \mathbf{v}^1 + \nabla_x \cdot \mathbf{v}^0] dv = 0.$$

From the divergence theorem, the periodicity and the adherence condition $(14c-\varepsilon^1)$ on Γ, the first term vanishes. Then, inverting $\mathbf{y}$-integration and $\mathbf{x}$-differentiation, we obtain

$$\nabla_x \cdot \left(\frac{1}{\Omega} \int_{\Omega_f} \mathbf{v}^0 d\Omega \right) = \nabla_x \cdot \langle \mathbf{v}^0 \rangle = 0,$$

where $\langle \mathbf{v}^0 \rangle$ is the Darcy velocity. Finally, the macroscopic description reads

$$\nabla_x \cdot \langle \mathbf{v}^0 \rangle = 0, \quad \langle \mathbf{v}^0 \rangle = -\frac{1}{\mu} \mathbf{K} \cdot \nabla_x P, \tag{19}$$

with

$$\mathbf{K} = \frac{1}{\Omega} \int_{\Omega_f} \mathbf{e}^i \otimes \mathbf{k}^i dv = \mathbf{K}^R + i\mathbf{K}^I, \tag{20}$$

where $\mathbf{K}^R$ and $\mathbf{K}^I$ are the real and imaginary parts of the complex dynamic permeability tensor $\mathbf{K}$. The inverse form of the macroscopic description is written,

$$\mu \mathbf{H} \cdot \mathbf{V} = -\nabla_x P, \quad \mathbf{H} = \mathbf{K}^{-1} = \mathbf{H}^R + i\mathbf{H}^I.$$

Overall equilibrium. The momentum balance of the fluid is not expressed by the Darcy law, since the viscous stresses are transferred to the skeleton. This appears by integrating $(16-\varepsilon^0)$ over the pores volume. Using the divergence theorem and the Ω-periodicity, we obtain

$$\int_\Gamma \boldsymbol{\sigma}^1 \cdot \mathbf{n} ds = \int_\Gamma [-p^1 \mathbf{I} + 2\mu \mathbf{D}_y(\mathbf{v}^0)] \cdot \mathbf{n} ds = \Omega_f \nabla_x P.$$

Thus the drag force of the flow is balanced by the skeleton. This overall equilibrium explicitly uses the periodicity to self-equilibrate the stress at the first order on the cell boundary, i.e.,

$$\int_{\partial\Omega_f - \Gamma} \boldsymbol{\sigma}^1 \cdot \mathbf{n} ds = \int_{\partial\Omega_f - \Gamma} [-p^1 \mathbf{I} + 2\mu \mathbf{D}_y(\mathbf{v}^0)] \cdot \mathbf{n} ds = 0. \tag{21}$$

Energy consistency. The energy consistency is derived [7] by taking the scalar product of the momentum balance with the conjugate of the fluid velocity $\overline{\mathbf{v}^0}$ (over bar stands for conjugate). After integrating over the pore, one obtains

$$-\langle \nabla_y p^1 \cdot \overline{\mathbf{v}^0} \rangle + \langle \nabla_y \cdot [2\mu \mathbf{D}_y(\mathbf{v}^0)] \cdot \overline{\mathbf{v}^0} \rangle = i\omega\rho \langle \mathbf{v}^0 \cdot \overline{\mathbf{v}^0} \rangle + \nabla_x P \cdot \langle \overline{\mathbf{v}^0} \rangle.$$

From the divergence theorem, the left hand side is transformed into

$$\langle p^1 \nabla_y \cdot \overline{\mathbf{v}^0} \rangle - 2\mu \langle \mathbf{D}_y(\mathbf{v}^0) : \mathbf{D}_y(\overline{\mathbf{v}^0}) \rangle + \frac{1}{\Omega} \int_{\partial\Omega_f} [-p^1 \mathbf{I} + 2\mu \mathbf{D}_y(\mathbf{v}^0)] \mathbf{n} \cdot \overline{\mathbf{v}^0} ds.$$

The surface integral vanishes because of the adherence on Γ and the periodicity on $\partial\Omega_f - \Gamma$. Accounting for the zero divergence of $\mathbf{v}^0$, we are left with the following identity:

$$2\mu \langle \mathbf{D}_y(\mathbf{v}^0) : \mathbf{D}_y(\overline{\mathbf{v}^0}) \rangle + i\omega\rho \langle \mathbf{v}^0 \cdot \overline{\mathbf{v}^0} \rangle = -\nabla_x P \cdot \langle \overline{\mathbf{v}^0} \rangle = \frac{1}{\mu} \nabla_x P \cdot \bar{\mathbf{K}} \cdot \overline{\nabla_x P} = \mu \mathbf{V} \cdot \mathbf{H} \cdot \bar{\mathbf{V}}, \tag{22}$$

which expresses the consistency of viscous and kinetic energy between the microscopic (left hand side) and macroscopic (right hand side) description. Note that this result explicitly uses the periodicity to state that

$$\int_{\partial\Omega_f - \Gamma} [-p^1 \mathbf{I} + 2\mu \mathbf{D}_y(\mathbf{v}^0)] \mathbf{n} \cdot \mathbf{v}^0 ds = 0. \tag{23}$$

Inversely, if equalities (21) and (23) are assumed, the energy consistency and the overall equilibrium are satisfied. It is then physically justified to transpose these necessary conditions (21) and (23) proven by homogenization of periodic media to the self-consistent scheme.

B. Consistent estimates of the dynamic permeability

1. Setting of the local permeability problem

The bicomposite sphere pattern (Fig. 3) is subjected to an uniform pressure gradient $\nabla P = \mathbf{G} = G\mathbf{e}_z$. Once again, we use spherical coordinates (r, θ, φ), with the origin at the center of the spheres and the $\theta = 0$ axis given by $\mathbf{e}_z$. The total pressure p is decomposed into the pressure $\mathbf{r} \cdot \mathbf{G}$ induced by the macroscopic gradient, and an additional pressure denoted $\tilde{p}$. The local flow of the fluid in the shell, $R_s = \beta R < r < R$ is driven by equations identical to that treated by homogenization for periodic media except for the periodicity conditions on $\tilde{p}$ and $\mathbf{v}$. These periodic conditions are replaced by the overall equilibrium [Eq. (21)] and energy consistency constraints [Eq. (23)]. Thus, we have

$$-\nabla(\tilde{p} + \mathbf{r} \cdot \mathbf{G}) + \Delta(\mu \mathbf{v}) = i\omega\rho \mathbf{v} \quad \text{in } \Omega_f, \tag{24a}$$

$$\nabla \cdot \mathbf{v} = 0 \quad \text{in } \Omega_f, \tag{24b}$$

$$\mathbf{v}(\beta R) = 0 \quad \text{on } \Gamma, \tag{24c}$$

$$\int_{\partial\Omega_f - \Gamma} [-\tilde{p}\mathbf{I} + 2\mu \mathbf{D}(\mathbf{v}] \cdot \mathbf{n} ds = 0 \quad \text{on } \partial\Omega, \tag{24d}$$

$$\int_{\partial\Omega_f-\Gamma}[-\tilde{p}\mathbf{I}+2\mu\mathbf{D}(\mathbf{v})]\mathbf{n}\cdot\mathbf{v}ds=0 \quad \text{on} \quad \partial\Omega. \tag{24e}$$

Following the HPM results, the macroscopic behavior complies with the dynamic Darcy law [Eq. (19)]. The Darcy velocity and the isotropic dynamic permeability tensor $\mathbf{K}=\mathcal{K}\mathbf{I}$, are derived from the relationships,

$$\mathbf{V}=\frac{1}{\Omega}\int_{\Omega_f}\mathbf{v}dv, \quad \mathbf{V}=-\frac{1}{\mu}\mathbf{K}\cdot\mathbf{G}.$$

2. Three estimates of dynamic permeability

From classical algebra, the general form of $\tilde{p}$ and $\mathbf{v}$ respecting the isotropy of space and satisfying the Navier-Stokes equation and the incompressibility are

$$p=\mathbf{G}\cdot\nabla h(r), \quad \mu\mathbf{v}=\mathbf{G}\cdot[\nabla\otimes\nabla f-\mathbf{I}\triangle f], \tag{25}$$

where

$$h(r)=c_0\frac{r^2}{6}-c_1\frac{1}{r}, \tag{26}$$

$$f(r)=\delta_v^2\left[c_0\frac{r^2}{12}+c_1\frac{1}{r}+\delta_v^2\left(c\frac{e^{r/\delta_v}}{r/\delta_v}+c'\frac{e^{-r/\delta_v}}{-r/\delta_v}\right)\right]. \tag{27}$$

The constants (c_0,c_1,c',c) are determined using the adherence, the overall equilibrium and energy consistency conditions (24b)–(24d). The energy condition, apparently nonlinear, requires a specific analysis. In this aim, note first from Eq. (25), that the radial velocity reads

$$v_r=-\frac{2f'}{r}\frac{\mathbf{G}}{\mu}\cdot\mathbf{e}_r.$$

Hence, as the mean velocity (of zero divergency) defines the Darcy velocity, we have:

$$\mathbf{V}=\langle\mathbf{v}\rangle=\frac{1}{\Omega}\int_{\partial\Omega_f}\mathbf{r}(\mathbf{v}\cdot\mathbf{e}_r)ds=-2\frac{f'(R)}{R}\frac{\mathbf{G}}{\mu}.$$

Then, $V_r(R)=v_r(R)$, i.e., the radial components of the Darcy velocity and the local fluid velocity are identical at any point on the bicomposite sphere boundary. Now, introduce the Darcy velocity $\mathbf{V}$ to rewrite the energy consistency condition as

$$\int_{\partial\Omega_f-\Gamma}\{[-\tilde{p}\mathbf{I}+2\mu\mathbf{D}(\mathbf{v})]\cdot\mathbf{e}_r\}\cdot[\mathbf{v}-\mathbf{V}]ds + \mathbf{V}\cdot\int_{\partial\Omega_f-\Gamma}\{[-\tilde{p}\mathbf{I}+2\mu\mathbf{D}(\mathbf{v})]\cdot\mathbf{e}_r\}ds=0.$$

The second integral vanishes because of the overall equilibrium and since $V_r(R)-v_r(R)=0$, we are left with

$$\int_{\partial\Omega_f-\Gamma}2\mu D_{r\theta}(\mathbf{v})[v_\theta-V_\theta]ds=0.$$

According to the field expressions, the energy consistency condition leads to the alternative:

(i) either the shear stress $2\mu D_{r\theta}$ vanishes uniformly and the stress vector at the boundary of the fluid inclusion match the Darcy pressure. This assumption leads to the *P-estimate*.

(ii) or the tangential velocities are equals, i.e., $v_\theta=V_\theta$ and the fluid and Darcy velocities are identical on the boundary, i.e., $\mathbf{v}(R)=\mathbf{V}(R)$. This assumption leads to the *V-estimate*.

Finally, the *C-estimate* results from the "cell" model assumption of vanishing vorticity at the boundary (e.g., Tarnow [17] and Umnova *et al.* [18]). This means that the fluid pressure (not the stress) at the boundary equals the Darcy pressure. Despite its nonconsistency, the C-assumption is of physical interest since, referring to the HPM, as the P-assumption, the C-boundary conditions are correct up to the first order, conversely to the V-boundary conditions.

According to the P-, V-, and C-assumption, the resolution of the three linear systems allows the determination of the three dynamic permeability estimates whose expressions are given hereafter [16].

(i) The P-estimate reads, where $x=R/\delta_v$,

$$K_p=\frac{\delta_v^2}{1-\frac{3}{x^2}C_p}, \quad C_p=\frac{A_p+B_p\tanh[x(\beta-1)]/x}{a_p+b_p\tanh[x(\beta-1)]/x}, \tag{28}$$

with

$$A_p=[3+(\beta x)^2][1+x^2/6]-3\beta[1+x^2/2],$$

$$B_p=[3+(\beta x)^2][1+x^2/2]-3\beta x^2[1+x^2/6],$$

$$a_p=[3+(\beta x)^2]/3-3\beta-[1+x^2/6]2/\beta+\frac{4}{\cosh[x(\beta-1)]},$$

$$b_p=[3+(\beta x)^2]-\beta x^2-[1+x^2/2]2/\beta. \tag{29}$$

(ii) The V-estimate reads

$$K_v=\frac{\delta_v^2}{1-\frac{3}{x^2}C_v}, \quad C_v=\frac{A_v+B_v\tanh[x(\beta-1)]/x}{a_v+b_v\tanh[x(\beta-1)]/x}, \tag{30}$$

with

$$A_v=[3+(\beta x)^2]-3\beta[1+x^2/3],$$

$$B_v=[3+(\beta x)^2][1+x^2/3]-3\beta x^2,$$

$$a_v=-2[\beta+1/\beta]+\frac{4}{\cosh[x(\beta-1)]},$$

$$b_v=[3+(\beta x)^2]2/3-[1+x^2/3]2/\beta. \tag{31}$$

(iii) The C-estimate reads (this expression differs from that given by Umnova *et al.* [18]),

$$K_c=2\delta_v^2\left(1-\frac{1}{1-A_c}\right), \tag{32}$$

where

$$A_c=\frac{(1-\beta^3)}{3}+\frac{\beta^2}{x^2}\frac{1-1/\beta+(x^2-1/\beta)\tanh[(\beta-1)x]/x}{1+\tanh[(\beta-1)x]/x}.$$

C. Estimates versus numerical values on spheres and polyhedrons packings

To compare estimates and numerical values determined on the two families of periodic media, we successively consider the characteristic parameters:

(i) at low and high frequency in the whole range of porosity,

(ii) in the whole frequency range for a dilute concentration ϕ=0.7 and an higher concentration ϕ=0.3. In this latter case, spheres in (SC), (BCC), and (FCC) microstructures overlap.

1. Low frequency

In the quasistatic regime (low frequency), i.e., when $l/\delta_v \to 0$, viscous effects dominate the inertia. The homogenization for periodic media enables to establish that Auriault *et al.* [10],

$$H(\omega) \simeq \frac{1}{\mathcal{K}} + \frac{i\omega\rho}{\mu}\frac{\alpha_0}{\phi}, \tag{33}$$

where $\mathcal{K}$ is the intrinsic permeability, and α_0 the low-frequency tortuosity. Expanding the dynamic permeability estimates at low frequency gives a behavior in conformity to Eq. (33). The three intrinsic permeability estimates read [15]

$$\mathcal{K}_p = \frac{R^2}{3}\left[-1 + \frac{2+3\beta^5}{\beta(3+2\beta^5)}\right], \tag{34}$$

$$\mathcal{K}_v = \frac{R^2}{18}\left[4\frac{1-\beta}{\beta} - 5\frac{(1-\beta^2)^2}{1-\beta^5}\right], \tag{35}$$

$$\mathcal{K}_c = \frac{2R^2}{45}\left[\frac{5-9\beta+5\beta^3-\beta^6}{\beta}\right]. \tag{36}$$

The analytical expressions of α_0 which depends on β only, are rather complicated and not presented here.

The Fig. 5(a) shows the evolution of the dimensionless intrinsic permeability $\mathcal{K}/R_s^2$ of periodic arrays of spheres and polyhedrons, and the three self-consistent estimates versus the porosity. For periodic arrays, R_s is an equivalent radius of the solid inclusion estimated as follows: $R_s=[3(1-\phi)\Omega/(4\pi n)]^{1/3}$, where n is the number of inclusions in the REV. Figure 5(a) underlines the tremendous effect of the porosity on the intrinsic permeability and that the permeability of the periodic arrays is closer to P and C-estimates than to the V-estimate. For periodic array of polyhedrons, the agreement with the P and C-estimates is remarkable whatever the arrangement (then geometry of the solid inclusion) in the whole range of porosity. By contrast, we observe that for periodic arrays of spheres, the computed values slightly depend on the arrangement (conversely to fibrous media [13]) when the porosity is larger than 0.6. P and C-estimates appear as an accurate analytic approximation up to the maximum packing concentration [Fig. 5(b)]. Beyond, the geometry of the flow through overlapping spheres apart significantly from the smooth flow in the bicomposite pattern, and consequently the discrepancies increase.

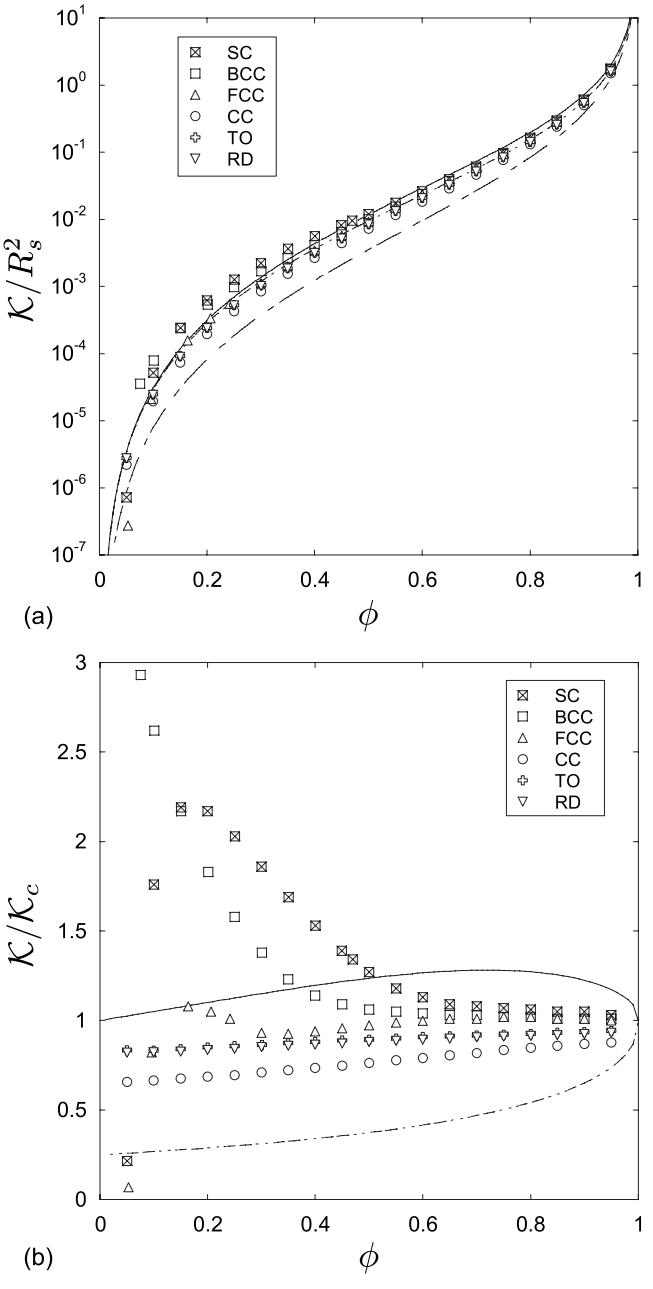

FIG. 5. (a) Dimensionless permeability $\mathcal{K}/R_s^2$ versus porosity ϕ. Comparison between estimates: $\mathcal{K}_p$ (continuous line), $\mathcal{K}_v$ (dashed line), $\mathcal{K}_c$ (mixed line) and numerical results for the different packings of spheres and polyhedrons (marks). (b) Ratios $\mathcal{K}_p/\mathcal{K}_c$ (continuous line), $\mathcal{K}_v/\mathcal{K}_c$ (dashed line) and numerical values $\mathcal{K}/\mathcal{K}_c$.

Figure 6 illustrates the sensitivity of the low-frequency tortuosity α_0 to the morphology of the media. Numerical values for the array of spheres (SC), (BCC), and (FCC) mainly track the P- and C-estimates when the porosity is larger than 0.6. Discrepancies are significant at lower porosity, and depend on the type of array. Note the good agreement between numerical values for arrays of polyhedrons and the P-estimate in the whole range of porosity.

2. High frequency

At high frequency, i.e., when $l/\delta_v \to \infty$, inertial effects dominate, and viscous effects are confined to a viscous layer.

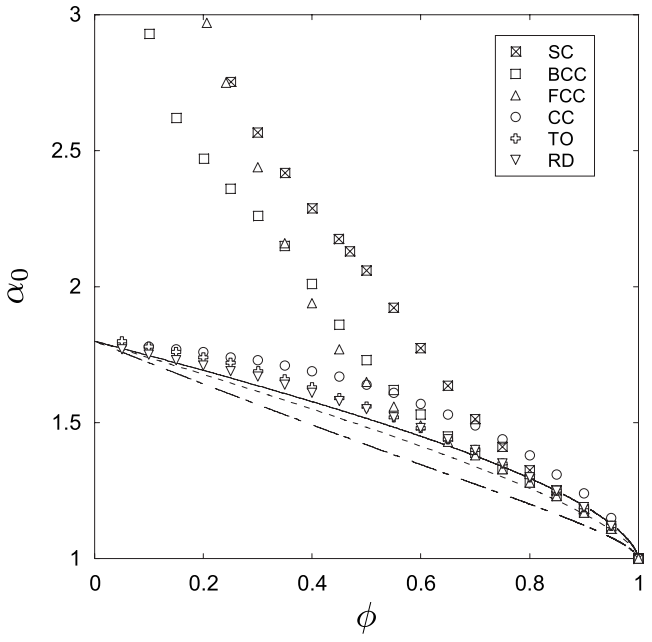

FIG. 6. Evolution of low-frequency tortuosity α_0 versus the porosity ϕ. Comparison between estimates: α_{0p} (continuous line), α_{0c} (dashed line), α_{0v} (mixed line) and numerical results for the different packing of spheres and polyhedrons (marks).

The HPM enables to establish that Auriault *et al.* [10],

$$\frac{\mu}{i\omega\rho}H(\omega)\phi \simeq \alpha_\infty\left(1+\sqrt{\frac{M}{2}\frac{\omega_c}{i\omega}}\right), \tag{37}$$

where α_∞ is the tortuosity, M is a shape factor and ω_c is the critical frequency delimiting the low- and high-frequency domains. This latter, which is obtained by equalizing viscous and inertial effects of the macroscopic flow, reads

$$\omega_c = \frac{\phi\mu}{\mathcal{K}\rho\alpha_\infty}.$$

Following Johnson *et al.*[24], $\sqrt{(M/2)(\omega_c/i\omega)}$ may also be expressed as $2\delta_v/\Lambda$, where Λ is the characteristic viscous length of the medium. The high-frequency behavior derived by expanding the dynamic permeabilities estimates complies with Eq. (37). As for the tortuosity, the P, V, and C-estimates lead to the same value,

$$\alpha_{\infty p,v,c} = 1+\beta^3/2 = \frac{3-\phi}{2} < \alpha_{0v} < \alpha_{0c} < \alpha_{0p}. \tag{38}$$

This is consistent with the fact that, at high frequency, the viscous effects are much smaller than the inertia. Thus, α_∞ may be derived from a perfect fluid flow, where the interface conditions involve only the radial component $\mathbf{v}\cdot\mathbf{n}$, which is independent on the P-, V- or C-assumption as mentioned previously. Note also that the perfect fluid problem is identical to the diffusion problem (Sec. III) where $\mathbf{v}$, p, and $1/i\omega\rho$, replace, respectively, the flux, the concentration and the diffusion coefficient (the motionless solid can be considered of infinite density, i.e., of zero diffusion). Therefore, in accordance with Eqs. (13) and (38),

$$\frac{\alpha_{\infty p,v,c}}{\phi} = \frac{D}{\tilde{D}} = \frac{3-\phi}{2\phi}.$$

As for the form factors, high-frequency expansions give

$$M_p = 2\left[\frac{9\beta^2}{2\phi^2}\right]^2\frac{\phi\mathcal{K}_p}{\alpha_\infty R^2}, \tag{39}$$

$$M_v = 2\left[\frac{9(\beta^2+\beta^6)}{2\phi^2}\right]^2\frac{\phi\mathcal{K}_v}{\alpha_\infty R^2}, \tag{40}$$

$$M_c = 2\left[\frac{9\beta^3}{2\phi^2}\right]^2\frac{\phi\mathcal{K}_c}{\alpha_\infty R^2}. \tag{41}$$

Figure 7 depicts the dependence of the high-frequency tortuosity α_∞ and the form factor M on the porosity. Once again, the tortuosity of polyhedron arrays is well described by the self-consistent estimates in the whole range of porosity while for array of spheres, good agreement is only observed for porosities larger than 0.6. The same remarks apply to the form factor M. For polyhedron arrays, M lies in between the P- and C-estimates. For array of spheres, M presents a maximum for porosities corresponding to the maximum packing before overlapping. By comparison with the polyhedron arrays, this result means that the disturbance on the flow due to the solid percolation induces a large increase in the viscous dissipation.

Figure 8 shows the evolution of the dimensionless characteristic viscous length Λ/R_s versus the porosity. Once again, we observe excellent agreement between the P-estimate and numerical values of polyhedron arrays in the whole range of porosity. Numerical values for periodic array of nonoverlapping spheres lies between the P and C-estimates. When spheres overlap, as for the intrinsic permeability, the P-estimate underestimates numerical values.

3. Whole frequency range

The dimensionless terms $K/\mathcal{K}$ and $H\phi\mu/(i\omega\rho\alpha_\infty) = H\mathcal{K}\omega_c/\omega$ depend only on the dimensionless frequency ω/ω_c. Concerning the variation of H versus frequency, it may also be demonstrated [16] that

$$\frac{dH^R}{d\omega} > 0 \quad \text{and} \quad \frac{d(H^I/\omega)}{d\omega} < 0. \tag{42}$$

Using the low- and high-frequency limits, the P-, V-, and C-equivalent media present different critical frequencies,

$$\omega_{ci} = \frac{\mu\phi}{\mathcal{K}_i\rho\alpha_\infty}, \quad i=p,v,c.$$

Figures 9(a) and 9(b) underline the influence of the morphology and of the ratio ω/ω_c on the intensity of the microscopic velocity field $\mathbf{v}^0$ deduced from numerical simulations on 1/16 of body-centered cubic arrays of truncated octahedrons (TO) and of spheres (BCC) with a porosity ϕ=0.25 and when the macroscopic gradient $\mathbf{G}$ is along $\mathbf{z}$. In both microstructures, as expected, we observe that by increasing ω/ω_c, inertial effects dominate and viscous effects are mainly confined to a

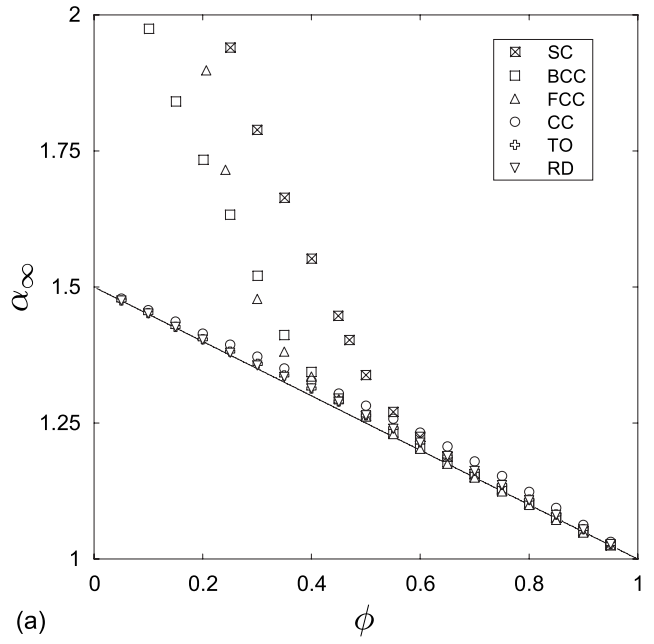

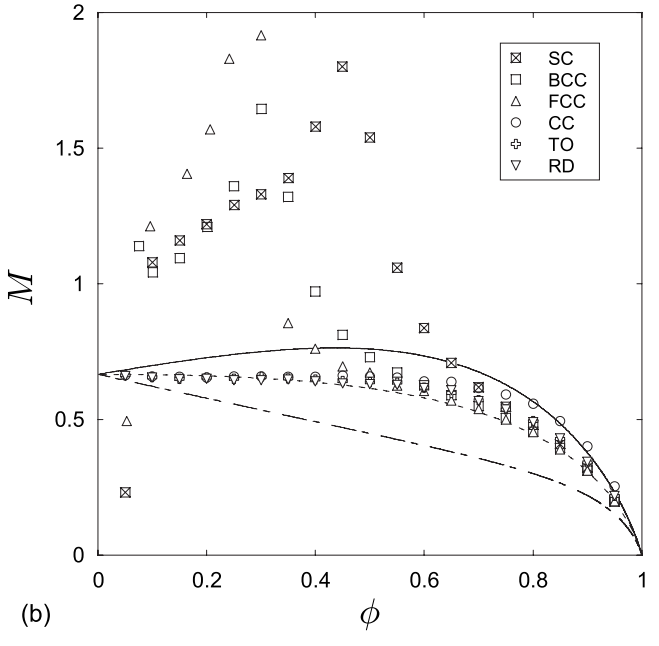

FIG. 7. (a) High-frequency tortuosity α_∞ versus porosity ϕ. Comparison between estimates: $\alpha_{\infty p,c,v}$ (continuous line) and numerical results for the different packings of spheres and polyhedrons (marks). (b) Form factor M versus porosity ϕ. Comparison between estimates: M_p (continuous line), M_c (dashed line), M_v (mixed line) and numerical results for the different packings of spheres and polyhedrons (marks).

thin viscous layer. These figures also clearly highlight that at low and high frequencies, the intensity of the flow is maximum in channels almost parallel to the macroscopic gradient of pressure and minimum (almost zero) otherwise (when the wall of channels are perpendicular to the flow). Finally, notice that the flow in the periodic array of spheres (BCC) is strongly affected by the overlapping areas, and consequently the dynamic permeability is significantly affected.

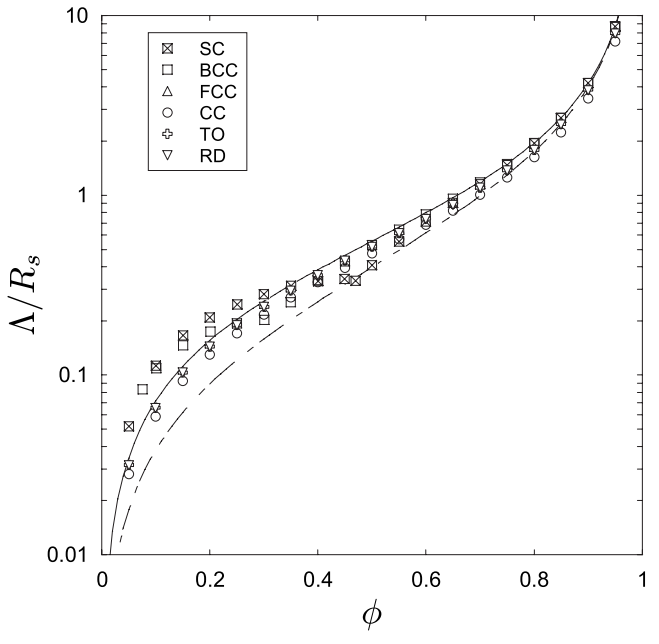

FIG. 8. Dimensionless viscous length Λ/R_s versus porosity ϕ. Comparison between estimates: Λ_p (continuous line), Λ_v (mixed line) and numerical results for the different packings of spheres and polyhedrons (marks).

Figures 10 and 11 present the dependence of the dimensionless real and imaginary part of **H** on the dimensionless frequency ω/ω_c, when the porosity is equal to 0.7 and 0.3, respectively. When the porosity is large, Fig. 8 shows that P and C-estimates mainly track numerical results of the body-centered cubic and face centered cubic arrays of spheres and polyhedrons in the whole dimensionless frequency range. Discrepancies between numerical results and estimates are much pronounced for the simple cubic array of sphere and polyhedrons. When the porosity is small, we still observe on Fig. 10 an excellent agreement between P and C-estimates and numerical values for the arrays polyhedrons in the whole dimensionless frequency range, especially for the arrays and the arrays of rhombic dodecahedrons (RD). As expected, for periodic arrays of spheres, the discrepancies with estimates are more significant in whole frequency range.

In conclusion, qualitatively, the three estimates describes rather well the features of the considered periodic arrays. Quantitatively, the C and P estimates are more accurate in the whole frequency range. For array of spheres, the accuracy is fairly good for the four parameters ($\mathcal{K}$, α_0, α_∞, M) when the sphere do not overlap (porosity larger than 0.6). For lower porosity, discrepancy up to a factor of around 2 may be observed. For polyhedron arrays results are in good agreement with P and C estimates whatever the porosity, consistently with the intuition that the flow through those arrays is geometrically close to the flow through the bicomposite spherical pattern.

V. THERMAL PERMEABILITY AND TRAPPING CONSTANT

Zwikker and Kosten [1] showed that in the harmonic regime the apparent compressibility of a gas in a porous me-

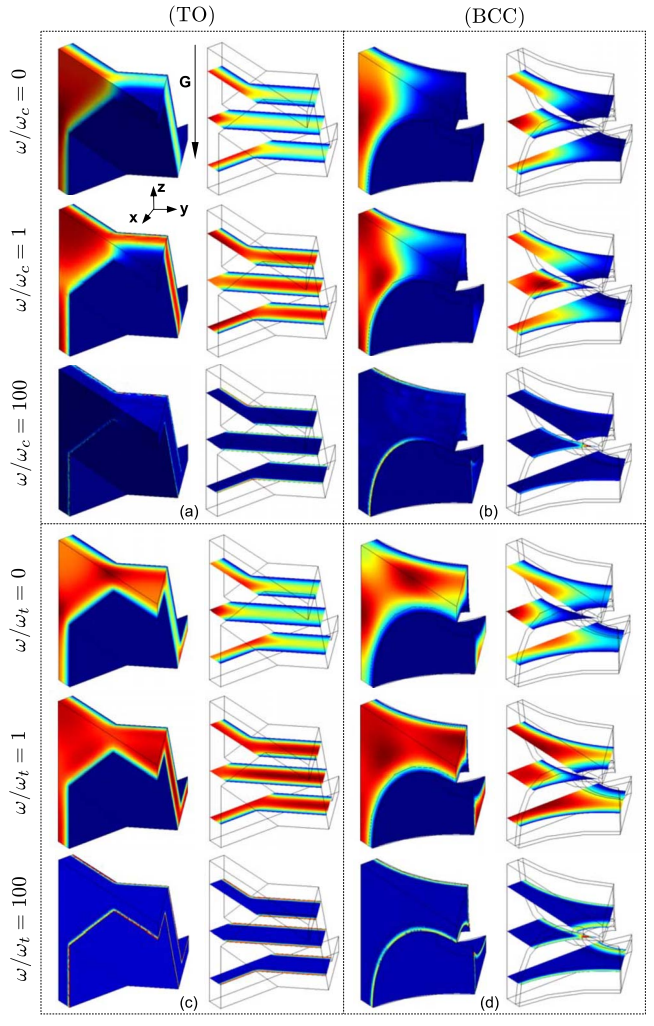

FIG. 9. (Color online) Color on line. Influence of the ratio ω/ω_c (resp. ω/ω_t) on the microscopic velocity field $\mathbf{v}^0$ (respectively, the local temperature field T^0) when the porosity ϕ=0.25 in packing of polyhedrons (a) [respectively, (c)] and spheres (b) [respectively, (d)]. The intensity varies between 0 (in blue) and a maximum value (in red).

dium involves local heat transport effects between the gas and the matrix. This local effect is described macroscopically by the thermal permeability. In steady state regime, this problem is closely related to the determination of the trapping constant, widely used for chemical processes in porous media. It describes the diffusive transport of a solute generated by a homogeneous source and absorbed instantaneously by the solid matrix [25].

A. Thermal permeability derived by homogenization

Homogenization leads to a macroscopic law for a gas subjected to a harmonic acoustic pressure P which has the following form:

$$\mathrm{div}(V) + \phi\mathcal{C}(\omega)[i\omega\phi P] = 0,$$

with

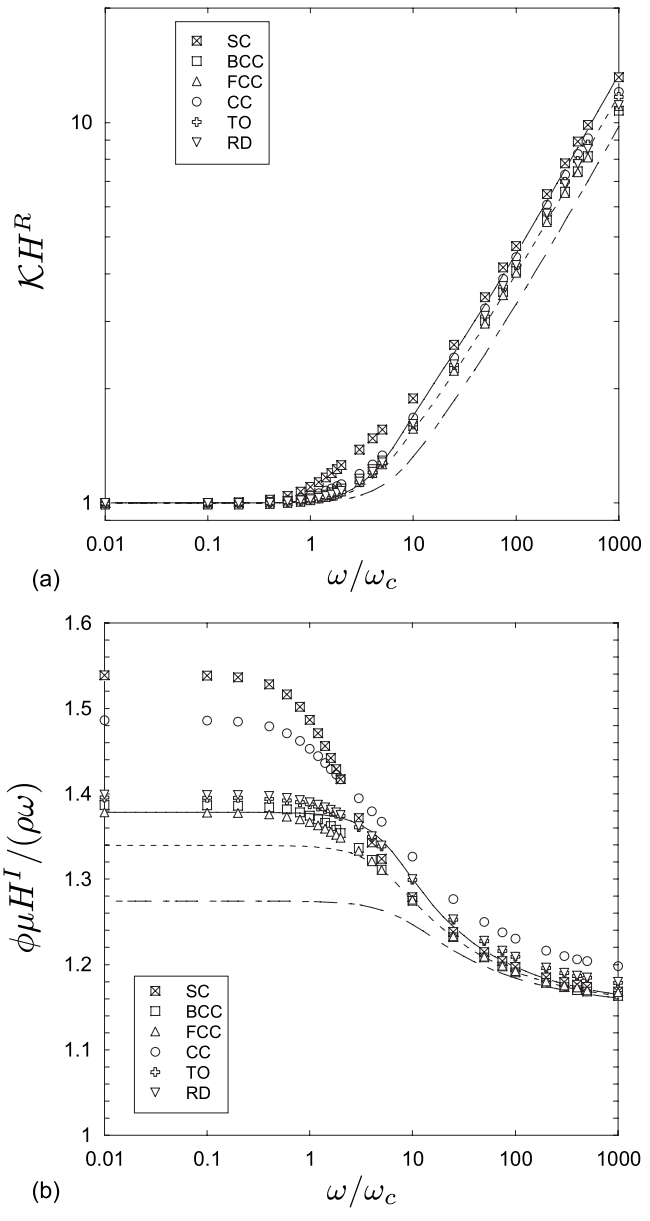

FIG. 10. Dimensionless real and imaginary part of $\mathbf{H}$ versus ω/ω_c when the porosity ϕ=0.7. Comparison between estimates: P-estimate (continuous line), C-estimate (dashed line), V-estimate (mixed line) and numerical results for the different packings of spheres and polyhedrons (marks).

$$\mathcal{C}(\omega) = \frac{1}{P^e}\left[1 - \frac{i\omega\rho^e C_p}{\lambda}\left(1 - \frac{1}{\gamma}\right)\Theta(\omega)\right],$$

where equilibrium values are indicated with the superscript ^{e}, λ is the thermal conduction coefficient of the gas, $\rho^e C_p$ is its heat capacity at constant pressure, and γ is the adiabatic constant. The coefficient $\Theta(\omega)$ which appears in the dynamic compressibility $\mathcal{C}(\omega)$ is known as the thermal permeability [4,26]. It originates from the heat transport in the gas in contact with the isothermal porous matrix, the thermal equilibrium being not achieved in the pores. Denoting the gas-solid temperature difference as T^0, the local problem is expressed through the transient Fourier equation in the gas, and

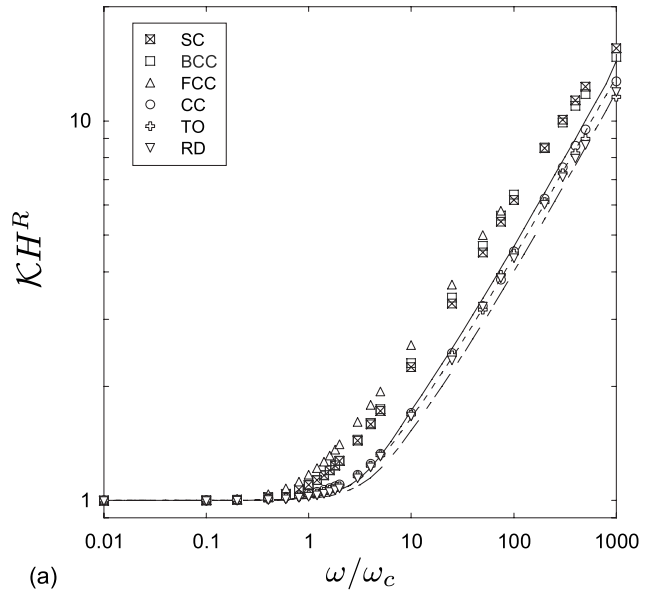

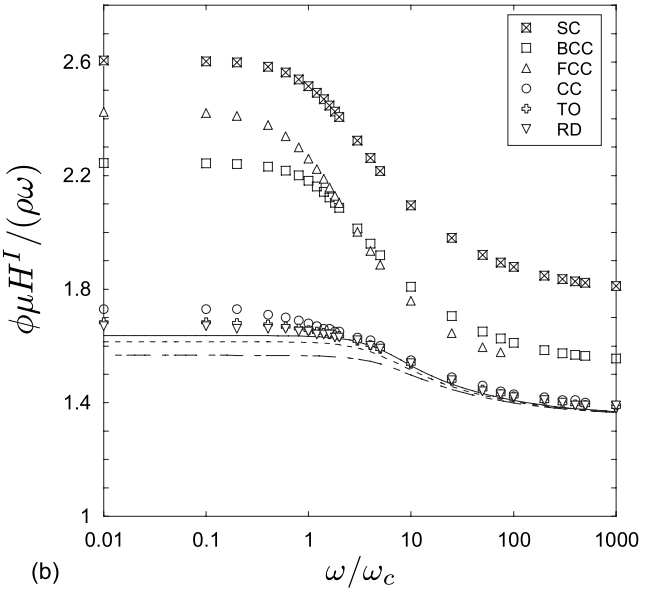

FIG. 11. Dimensionless real and imaginary part of **H** versus ω/ω_c when the porosity ϕ=0.3. Comparison between estimates: P-estimate (continuous line), C-estimate (dashed line), V-estimate (mixed line) and numerical results for the different packings of spheres and polyhedrons (marks).

the isothermal condition at the solid interface [6,27], where T^0 is Ω-periodic,

$$i\omega P - i\omega\rho^e C_p T^0 + \lambda\Delta_y T^0 = 0 \quad \text{on } \Omega_f, \tag{43a}$$

$$T^0 = 0 \quad \text{on } \Gamma. \tag{43b}$$

This scalar problem resembles to the vectorial problem of the dynamic permeability. By analogy, the solution and the macro description are expressed in the form,

$$T^0 = \frac{\theta}{\lambda} i\omega P \quad \text{then} \quad \langle T^0\rangle = \frac{\phi\Theta}{\lambda} i\omega P, \tag{44}$$

with

$$\Theta = \frac{1}{\Omega_f}\int_{\Omega_f} \theta d\Omega, \tag{45}$$

where θ is the complex valued temperature distribution obtained when $i\omega P/\lambda$ is unitary, and which therefore satisfies,

$$1 - \frac{1}{\delta_t^2}\theta + \Delta_y(\theta) = 0,$$

where the (complex) thickness of the thermal boundary layer is $\delta_t = \sqrt{\lambda/(i\omega\rho^e C_p)}$.

Energy consistency. The energy consistency is derived by integrating over the pore the product of the local balance [Eq. (43a)] with the conjugate field $\overline{T^{(0)}}$. Using the divergence theorem, one obtains

$$\frac{1}{\Omega}\int_{\partial\Omega_f} [\lambda\nabla_y T^0\cdot\mathbf{n}]\overline{T^0} ds + \langle\lambda\nabla_y T^0\cdot\nabla_y\overline{T^0}\rangle + i\omega\rho^e C_p\langle T^0\overline{T^0}\rangle = i\omega P\langle\overline{T^0}\rangle.$$

The surface integral vanishes because of the isothermal condition on Γ and of periodicity on $\partial\Omega-\Gamma$. Finally, replacing $\langle\overline{T^0}\rangle$ by its expression (44), we obtain

$$\langle\lambda\nabla_y T^0\cdot\nabla_y\overline{T^0}\rangle + i\omega\rho^e C_p\langle T^0\overline{T^0}\rangle = \omega^2\phi\frac{\bar{\Theta}}{\lambda}P\bar{P},$$

which expresses the consistency of the micro (left hand side) and macro (right hand side) descriptions. Once again this result explicitly uses the periodicity to state that

$$\int_{\partial\Omega_f-\Gamma} [\lambda\nabla_y T^0\cdot\mathbf{n}]\overline{T^0} ds = 0. \tag{46}$$

Link with trapping constant problem. The steady state trapping constant problem of a solute (concentration c, diffusion coefficient D), generated by an homogeneous source S in the pores and which is absorbed instantaneously when it comes in contact with the solid matrix is driven by the set,

$$S - D\Delta_y c^0 = 0 \quad \text{on } \Omega_f, \tag{47a}$$

$$c^0 = 0 \quad \text{on } \Gamma. \tag{47b}$$

By analogy with the set Eqs. (43a) and (43b), the mean concentration in the pores reads

$$\frac{c^0}{\phi} = \frac{\Theta(0)}{D}S. \tag{48}$$

Which gives, accounting for the usual definition of the trapping constant,

$$\Upsilon D\langle c^0\rangle/\phi = S, \quad \text{thus,} \quad \Upsilon = \frac{1}{\Theta(0)}. \tag{49}$$

B. Self-consistent estimate of the thermal permeability

The estimate of $\Theta(\omega)$, is determined on the bicomposite spherical pattern presented in Fig. 3. The temperature field $\tilde{\theta}$ in the shell, $\beta R < r < R$ is governed by equations identical to that treated by HPM Eqs. (43a) and (43b) except for the periodicity condition replaced here by the consistency constraint [Eq. (46)],

$$1 - \frac{i\omega\rho^e C_p}{\lambda}\tilde{\theta} + \Delta\tilde{\theta} = 0 \quad \text{in } \Omega_f(\beta R \le r \le R), \tag{50a}$$

$$\tilde{\theta} = 0 \quad \text{on } \Gamma(r = \beta R), \tag{50b}$$

$$\int_{\partial\Omega_f - \Gamma} [\lambda \nabla_y \tilde{\theta} \cdot \mathbf{n}] \bar{\bar{\theta}} ds = 0 \quad \text{on } \partial\Omega(r = R). \tag{50c}$$

Due to the spherical symmetry of the problem, the solution only depends on r. Integration of the Helmholtz equation with a constant forcing term gives the general form of the solution,

$$\tilde{\theta} = \delta_t^2 \left[1 + c\frac{e^{r/\delta_t}}{r/\delta_t} + c'\frac{e^{-r/\delta_t}}{-r/\delta_t} \right].$$

The determination of the constants c and c' requires two boundary conditions, which are the isothermal condition on the solid sphere [Eq. (50b)], i.e., $\tilde{\theta}(\beta R) = 0$, and the consistency condition (50c). This latter simply reads

$$(4\pi R^2)\lambda \tilde{\theta}'(R)\bar{\bar{\theta}}(R) = 0.$$

As a consequence, $\tilde{\theta}'(R) = 0$. The alternative $\tilde{\theta}(R) = 0$ would introduce an artificial isothermal condition not consistent with the local physics. The substitution of the expression for $\tilde{\theta}$ into $\tilde{\theta}(\beta R) = 0$ and $\tilde{\theta}'(R) = 0$, leads to a simple linear system, the solution to which allows us to determine θ. Integration of this field over the volume of the pores gives the following estimate of the thermal permeability:

$$\Theta_{sc}(\omega) = \delta_t^2 \left(1 - \beta^3 + \frac{3\beta}{x^2} \left[\beta x \frac{1 + x\tanh[x(\beta - 1)]}{x + \tanh[x(\beta - 1)]} - 1 \right] \right), \tag{51}$$

where $x = R/\delta_t$. The properties of $\Theta_{sc}(\omega)$ are very similar to those of the dynamic permeability which were discussed in the previous section. We also note the similarity of the analytical functions involved in Θ_{sc} and K_c. This stems from the close relationship between the scalar problem of thermal permeability and the vectorial problem of the dynamic permeability. For the spherical geometry, the condition of zero vorticity has an exact analog in the condition of zero thermal gradient, which allows to relate analytically the velocity and temperature fields.

C. Features of the thermal permeability

At low frequencies, i.e., when $l/\delta_t \to 0$, conduction dominates, and the gas is in the quasi-isothermal regime. The HPM enables to establish that

$$\Theta(\omega) \simeq \Theta(0)\left(1 - \frac{i\omega\rho^e C_p}{\lambda}\Theta(0)\zeta_0 \right), \tag{52}$$

where $\Theta(0)$ is the static thermal permeability and ζ_0 is the corrector coefficient for the low-frequency heat capacity. Expanding the thermal permeability estimates at low frequency gives a behavior in conformity to Eq. (52). The static thermal permeability and the trapping constant estimates are directly linked to the intrinsic permeability K_c given by Eq. (36),

$$\Theta_{sc}(0) = \frac{1}{\Upsilon_{sc}} = \frac{3K_c}{2\phi}.$$

The analytical expressions of ζ_0, which depends on β, only is written,

$$\zeta_{sc0} = \frac{5(1 + \beta + \beta^2)(35 + 49\beta + 30\beta^2 + 10\beta^3 + 2\beta^4)}{7(5 + 6\beta + 3\beta^2 + \beta^3)^2}.$$

At high frequencies, i.e., when $l/\delta_t \to \infty$, inertia dominates and the gas is in the quasi-adiabatic regime. Conductive effects are confined to the thermal boundary layer, implying that

$$\frac{\lambda}{i\omega\rho^e C_p \Theta(\omega)} \simeq 1 + \sqrt{\frac{M_t}{2}\frac{\omega_t}{i\omega}},$$

where ω_t is the critical frequency separating the low- and high-frequency domains. This is obtained by equating conductive effects (i.e., the low-frequency real part) and inertial effects (i.e., the high-frequency imaginary part) in $\Theta(\omega)$,

$$\omega_t = \frac{\lambda}{\Theta(0)\rho^e C_p}.$$

M_t is a form factor whose self-consistent estimate is

$$M_{tsc} = \frac{6(1 - \beta)^3\beta^3(5 + 6\beta + 3\beta^2 + \beta^3)}{5(1 - \beta^3)^3}.$$

Moreover, from Champoux and Allard [28],

$$\sqrt{\frac{M_t}{2}\frac{\omega_t}{i\omega}} = \frac{2\delta_t}{\Lambda_t},$$

where Λ_t is the characteristic thermal length in the medium, which, relative to the size of the solid sphere, has a self-consistent estimate of

$$\frac{\Lambda_{tsc}}{R_s} = \frac{2\phi}{3(1 - \phi)}.$$

Finally, in the whole frequency range, $\Theta(\omega)/\Theta(0)$ only depend on the dimensionless frequency ω/ω_t. Also, following the same reasoning as for the dynamic permeability, it can be shown that

$$\frac{d(\Theta^{-1})^R}{d\omega} \ge 0, \quad \frac{d((\Theta^{-1})^I/\omega)}{d\omega} \le 0.$$

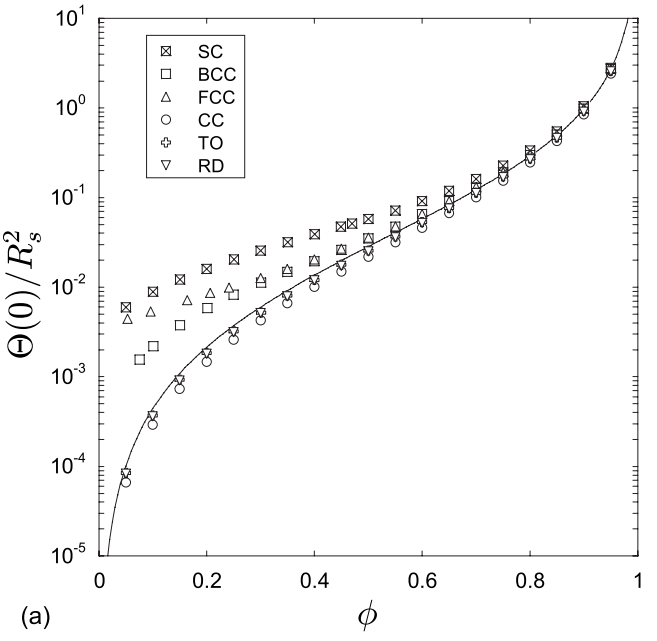

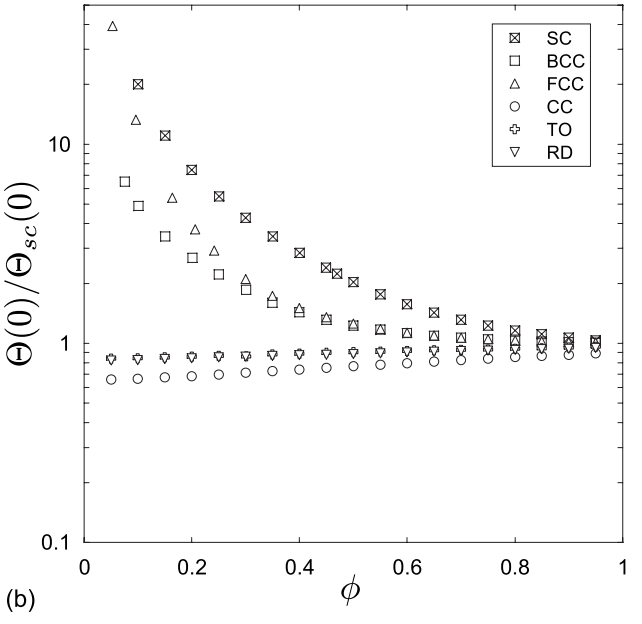

FIG. 12. (a) Dimensionless static thermal permeability $\Theta(0)/R_s^2$ versus porosity ϕ. Comparison between estimate $\Theta_{sc}(0)$ (continuous line), and numerical results for the different packings of spheres and polyhedrons (marks). (b) Ratio $\Theta(0)/\Theta_{sc}(0)$ versus porosity ϕ.

D. Estimates versus numerical values on spheres and polyhedrons packings

As for dynamic permeability, to compare the thermal permeability estimates and the numerical values determined on the two families of periodic media, we successively consider the parameters at low and high frequency for the whole range of porosity and the whole frequency range (for ϕ=0.7 and ϕ=0.3).

Figures 12–15 depict the influence of the morphology of the media and the porosity on the effective parameters at low and high frequencies, i.e., $\Theta(0)/R_s^2$, ζ_0, M_t, and Λ_t/R_s, respectively. These figures appeal similar comments to the dynamic permeability. Numerical results on arrays of polyhedrons are well described by the consistent estimate whatever the arrangement (then geometry of the solid inclusion) in the whole range of porosity. Conversely, large discrepancies occur between numerical results on array of spheres and self-consistent estimate when the porosity is lower that 0.6, i.e., before that spheres overlap.

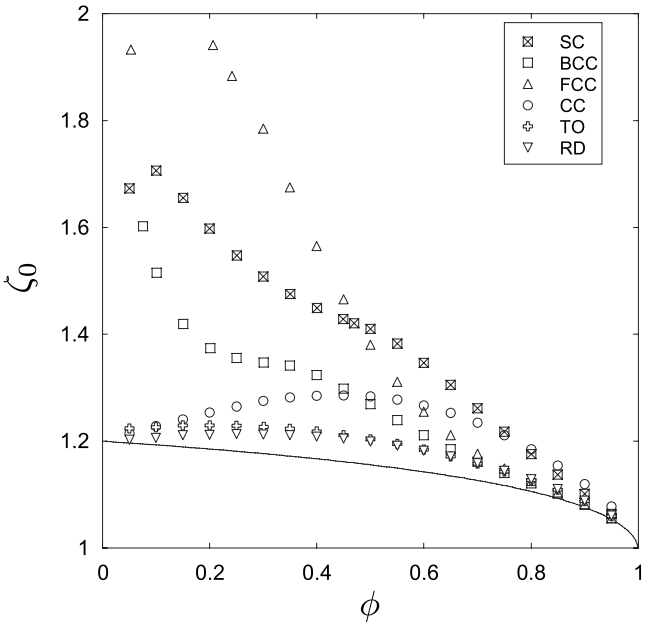

FIG. 13. Corrector for the low-frequency heat capacity ζ_0 versus porosity ϕ. Comparison between estimate ζ_{sc0} (continuous line) and numerical results for the different packings of spheres and polyhedrons (marks).

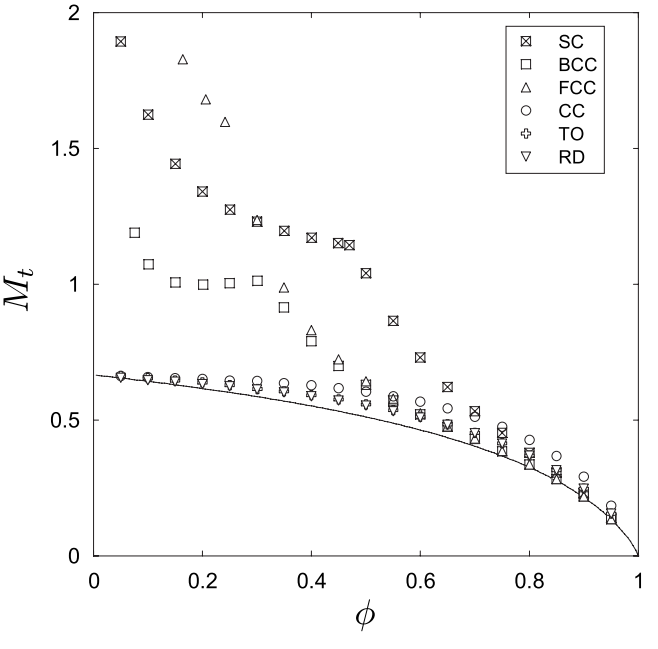

FIG. 14. Form factor M_t versus porosity ϕ. Comparison between estimate M_{tsc} (continuous line) and numerical results for the different packings of spheres and polyhedrons (marks).

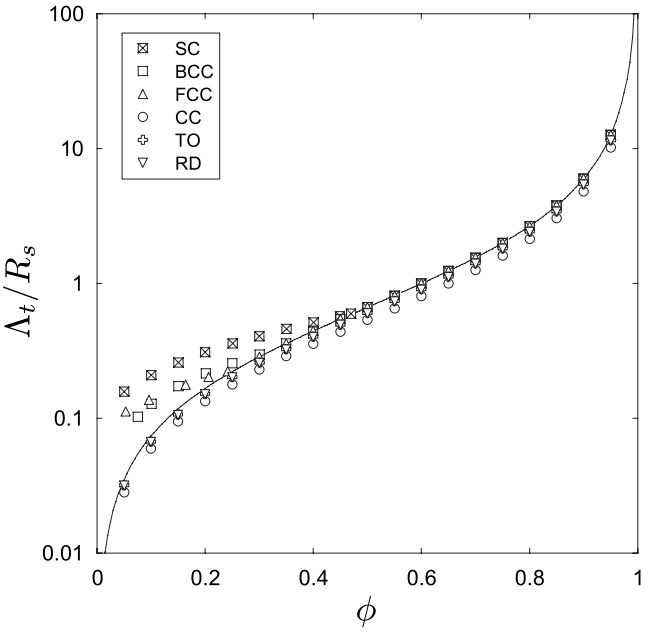

FIG. 15. Dimensionless viscous layer thickness Λ_t/R_s versus porosity ϕ. Comparison between estimate Λ_{tsc} (continuous line) and numerical results for the different packings of spheres and polyhedrons (marks).

Figures 16 and 17 present the dependence of the dimensionless real and imaginary part of $\Theta(\omega)$ on the dimensionless frequency ω/ω_t, when the porosity is equal to 0.7 and 0.3, respectively. All the comments already made in the case of the dynamic permeability remain valid for the thermal permeability. Whatever the porosity, Figs. 16 and 17 show rather good agreement between numerical results for arrays of polyhedrons [in particular (TO) and (RD)] and the self-consistent estimate. For periodic arrays of spheres, the discrepancies with estimate are more significant in whole frequency range and increase when the porosity decrease.

Note that the general trend is that the relative dispersion of the thermal permeability results is larger than for the dynamic permeability. This may be roughly explained by the fact that the isotropy of the scalar variable (the temperature) better surveys the microstructure than the oriented vectorial variable (the mass flux). This feature is illustrated in Figs. 9(c) and 9(d) which underline the influence of the morphology and of the ratio ω/ω_t on the intensity of the microscopic temperature field T^0 deduced from numerical simulations on 1/16 of body-centered cubic arrays of truncated octahedrons (TO) and of spheres (BCC) with a porosity ϕ=0.25. As for the flow, we observe that (i) in both microstructures by increasing ω/ω_t, inertial effects dominate and viscous effects are mainly confined to a thin viscous layer, and (ii) that the temperature field in the periodic array of spheres (BCC) is strongly affected by the overlapping areas. Moreover, theses figures also clearly underline that the microscopic temperature field (intensity and distribution) is, by contrast to the flow, independent of the orientation of the channel, and can be view as the superposition of the flow fields in the three main directions.

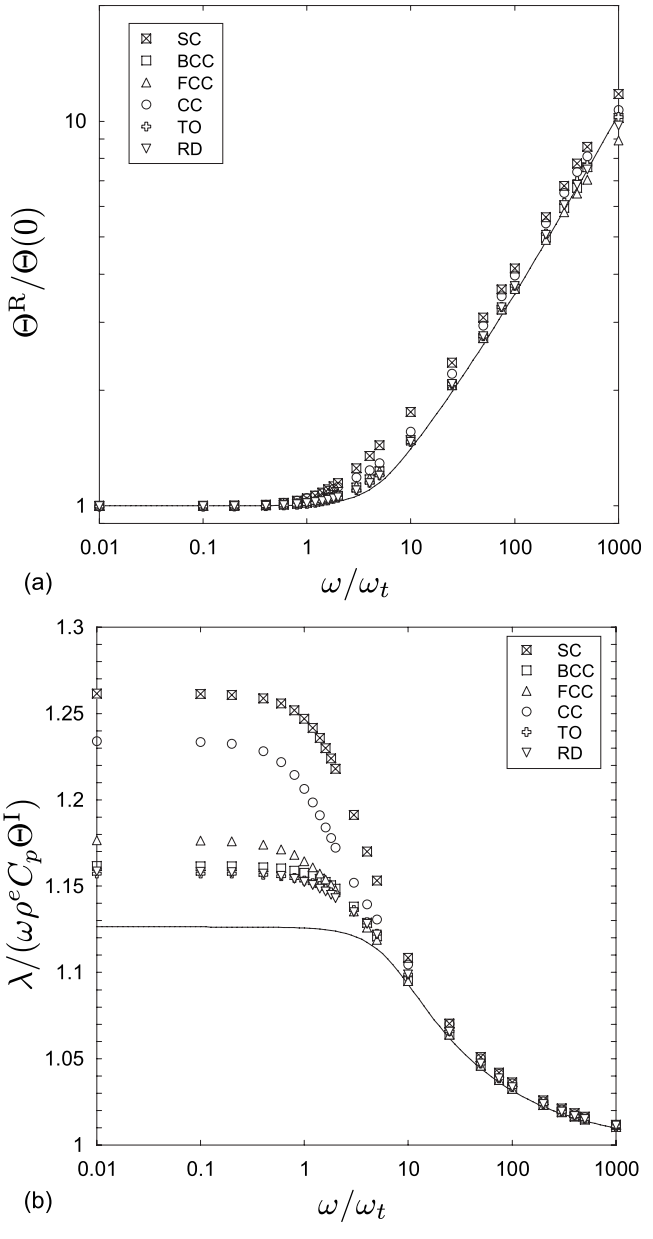

FIG. 16. Dimensionless real and imaginary part of Θ versus ω/ω_t when the porosity ϕ=0.7. Comparison between estimate (continuous line) and numerical results for the different packing of spheres and polyhedrons (marks).

VI. CONCLUSION

This paper exploits complementarily the homogenization of periodic media and the self-consistent scheme based on a bicomposite spherical pattern. This study emphasizes the common physical assumptions sustaining both approaches. By replacing the periodicity condition by a zero flux and energy through the surface of the pattern, the consistent solutions can be considered as geometrical approximations of the local problem derived through HPM, for periodic media of simple morphology. It is worth mentioning that the periodic and the substituted conditions are not equivalent. This is clearly evidenced by the fact that, conversely to the unicity of the solution provided by HPM, the SCM scheme leads in

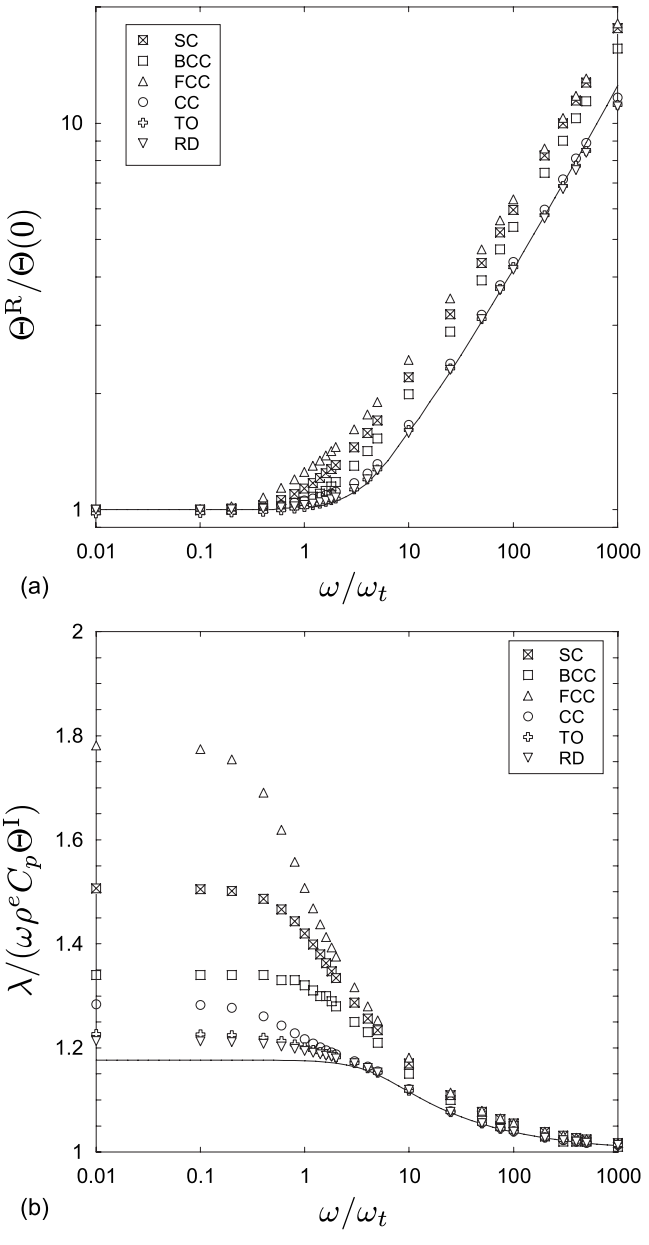

FIG. 17. Dimensionless real and imaginary part of Θ versus ω/ω_t when the porosity ϕ=0.3. Comparison between estimate (continuous line) and numerical results for the different packing of spheres and polyhedrons (marks).

principle to two solutions (one of them could be nonphysical). Despite this drawback the reliability of this procedure has been demonstrated on three different problems of transport. It can also be extended to other physics [29], for instance to assess the Klinkenberg effect, the inner heat transport with conducting skeleton, the diffusion with adsorption, the static or transient trapping coefficient, the permeability to linear viscoelastic saturating fluids, etc.

From the three treated examples, it appears that the bicomposite sphere estimates provide excellent analytical approximations of the effective parameters of periodic packing of polyhedrons on the *whole range of porosity*, especially for the array of truncated octahedrons (TO) and the array of rhombic dodecahedrons (RD). This stems from the fact that

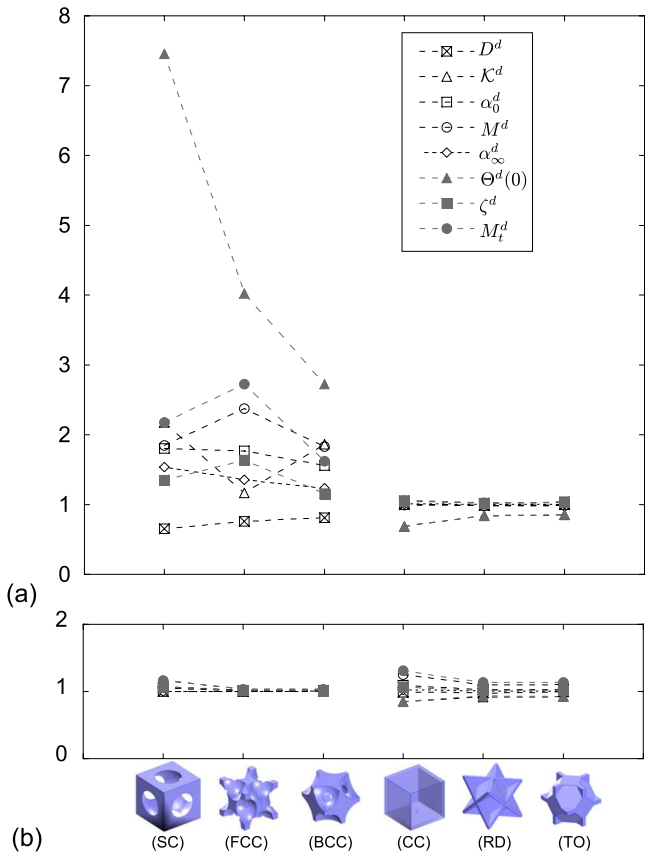

FIG. 18. (Color online) Dimensionless effective parameters (numerical value/consistent estimate) versus the morphology. (a) ϕ =0.2, (b) ϕ=0.8. With $D^d=D/\tilde{D}$, $\mathcal{K}^d=\mathcal{K}/\mathcal{K}_c$, $\alpha_0^d=\alpha_0/\alpha_{0c}$, $M^d=M/M_c$, $\alpha_\infty^d=\alpha_\infty/\alpha_{\infty c}$, $\Theta^d(0)=\Theta(0)/\Theta_{sc}(0)$, $\zeta_0^d=\zeta_0/\zeta_{0sc}$, $M_t^d=M_t/M_{tsc}$.

the geometry of the flow around polyhedrons is quite similar to the flow occurring on the bicomposite spherical pattern. As for the array of spheres, when $\phi>0.6$, the agreement with estimates is excellent, and is still reasonable otherwise. The increasing discrepancies for lower porosity is related to the change in the flow pattern, passing from a "smooth" field around nonoverlapping spheres, to a "highly" variable field through the corrugated channels in between the overlapping spheres. This phenomenon does not exist for polyhedrons packing, which explain the better agreement.

Meanwhile the bicomposite spherical pattern is an extremely simple and regular 3D pore geometry, the results underline the sensitivity of the macroscopic parameters to the morphology of the medium. This is illustrated on Fig. 18 for two values of the porosity. The parameters associated to the thermal flow [$\Theta(0)=1/\Upsilon$, M_t] are more sensitive to the morphology than those related to the viscous flow ($\mathcal{K}$,M), the less sensitive being those involve in inertial effects (α_0, α_∞, ζ_0).

Nevertheless such a geometry is not sufficient to capture the all complexity of the flow in actual geometry as illustrated by the effect of overlapping spheres. For this reason, the estimates may apply to porous media whose pores are sufficiently regular, but should be used cautiously otherwise.

[1] C. Zwikker and W. Kosten, *Sound Absorbing Materials* (Elsevier, Amsterdam, 1949).
[2] M. Biot, J. Acoust. Soc. Am. **28**, 168 (1956).
[3] D. Johnson, J. Koplik, and L. Schwartz, Phys. Rev. Lett. **57**, 2564 (1986).
[4] J.-F. Allard, *Propagation of Sound in Porous Media* (Elsevier Applied Science, England, 1993).
[5] J.-L. Auriault and E. Sanchez-Palencia, J. Mec. **16**, 576 (1977).
[6] E. Sanchez-Palencia, *Lectures Notes in Physics* (Springer-Verlag, Berlin, 1980), Vol. 127.
[7] J.-L. Auriault, Int. J. Eng. Sci. **18**, 775 (1980).
[8] A. S. Sangani and A. Acrivos, Int. J. Multiphase Flow **8**, 193 (1982).
[9] A. Chapman and J. Higdon, Phys. Fluids A **4**, 2099 (1992).
[10] J.-L. Auriault, L. Borne, and R. Chambon, J. Acoust. Soc. Am. **77**, 1641 (1985).
[11] M.-Y. Zhou and P. Sheng, Phys. Rev. B **39**, 12027 (1989).
[12] I. Malinouskaya, V. Mourzenko, J. Thovert, and P. Adler, Phys. Rev. E **77**, 066302 (2008).
[13] A. L. Berdichevsky and Z. Cai, Polym. Compos. **14**, 132 (1993).
[14] M. Thiery and C. Boutin, *Poromechanics II*, edited by J. Auriault *et al.* (Balkema, The Netherlands, 2002), pp. 575–581.
[15] C. Boutin, Eur. J. Mech. A/Solids **19**, 603 (2000).
[16] C. Boutin and C. Geindreau, J. Acoust. Soc. Am. **124**, 3576 (2008).
[17] V. Tarnow, J. Acoust. Soc. Am. **100**, 3706 (1996).
[18] O. Umnova, K. Attenborough, and K. M. Li, J. Acoust. Soc. Am. **107**, 3113 (2000).
[19] J.-L. Auriault, Int. J. Eng. Sci. **29**, 785 (1991).
[20] Z. Hashin, J. Compos. Mater. **2**, 284 (1968).
[21] R. M. Christensen and K. H. Lo, J. Mech. Phys. Solids **27**, 315 (1979).
[22] J.-P. Boelher, *Applications of Tensor Functions in Solid Mechanics*, CISM Courses and Lectures (Springer-Verlag, Wien, NY, 1987).
[23] T. Levy, Int. J. Eng. Sci. **17**, 1005 (1979).
[24] D. L. Johnson, J. Koplik, and R. Dashen, J. Fluid Mech. **176**, 379 (1987).
[25] S. Torquato, Phys. Rev. Lett. **64**, 2644 (1990).
[26] D. Lafarge, P. Lemarinier, J. F. Allard, and V. Tarnow, J. Acoust. Soc. Am. **102**, 1995 (1997).
[27] C. Boutin, P. Royer, and J.-L. Auriault, Int. J. Solids Struct. **35**, 4709 (1998).
[28] Y. Champoux and J.-F. Allard, J. Appl. Phys. **70**, 1975 (1991).
[29] J.-L. Auriault, C. Boutin, and C. Geindreau, *Homogenization of Coupled Phenomena in Heterogeneous Media* (Wiley-ISTE, London, 2009).